THE INTERNAL STRUCTURE OF NEPHRITE: EXPERIMENTAL AND COMPUTATIONAL EVIDENCE FOR THE COEXISTENCE OF MULTIPLE-CHAIN SILICATES WITHIN AN AMPHIBOLE HOST

By L. G. MALLINSON,† D. A. JEFFERSON,† J. M. THOMAS,† F.R.S., and J. L. HUTCHISON‡

† *Department of Physical Chemistry, University of Cambridge, Lensfield Road, Cambridge CB2 1EP, U.K.*

‡ *Department of Metallurgy and Science of Materials, University of Oxford, Parks Road, Oxford OX1 3PH, U.K.*

(*Received* 26 *January* 1979 – *Revised* 24 *May* 1979)

[Plates 1–16]

CONTENTS

PAGE

1. Introduction 538

2. Experimental 541

3. Computation of images for ideal and faulted tremolite and actinolite 542

4. Results 543
   (*a*) Experimental and calculated images of nephrite 543
   (*b*) Computer images of defect structures 545
   (*c*) Characterization of planar defect structures on (010) 545
      (i) Triple chain defects 545
      (ii) Single chain defects 546
      (iii) Quadruple chain defects 546
      (iv) Quintuple chain defects 546
      (v) Sextuple chain defects 546
      (vi) Extensive disorder 546
      (vii) Regular triple chain structure 547
      (viii) Terraced defects 548
      (ix) Defect terminations and dislocations 548

5. Summary and conclusions 550

References 551

 [Published 29 February 1980

Ultra-structural variations in samples of nephrite jade have been elucidated by a combination of high resolution electron microscopy, which explores local structure in a direct, 'real space' manner, and computational procedures using the so-called 'multislice' approach which enables the image generated under a given set of electron-optical conditions to be calculated as a function both of unit cell content and of specimen thickness. Microanalyses by electron-stimulated X-ray emission and by optical diffractometry (of micrographs) were also used.

Planar faults on (010) occur frequently in nephrite. These are of several distinct kinds, all of which have been characterized. The host amphibole, consisting of double chains of linked SiO_4 tetrahedra, is shown frequently to accommodate triple-chain lamellae which are coherently attached to the double-chain matrix on (010) planes. These triple-chain faults may occur in isolated fashion, but sometimes are arranged recurrently, in a disordered manner, within the amphibole host. The nephrite may also accommodate extended regions of a new, triple-chain mineral structure, the maximum observed width of this coexistent phase being *ca.* 340 Å. Other planar faults, composed of regions with chain widths ranging from one to six SiO_4 tetrahedra, have been detected and fully identified on the basis of the correspondence between theoretically calculated and observed images.

Detailed structural drawings for the continuous planar faults, as well as others that are described, are given. It is shown that edge-sharing of tetrahedra probably occurs close to the termini of certain types of discontinuous fault and that, in other cases of defect termination, screw-type dislocations may be incorporated to preserve the strain-free, structural regularity of the host.

It has not yet proved possible, with currently available *in situ* X-ray microanalytical techniques, to assign chemical compositions to the new structural types that have been brought to light by this study.

1. Introduction

After Wadsley (1964, 1970) had introduced the concept of the so-called crystallographic shear (CS) plane† to account for the observed properties of certain oxygen-deficient metal oxides, it soon became apparent (Bursill & Hyde 1972; Anderson & Tilley 1974) that planar faults probably predominate over other structural irregularities, especially point defects, in many grossly non-stoichiometric systems. The concept itself has served as an invaluable, unifying principle in the structural chemistry of binary and ternary metal oxides which display a remarkable (sometimes infinitely adaptive) capacity (see Anderson 1973; Kittel 1978) to exhibit seemingly anomalous stoichiometries. Regularly spaced CS planes lead to specific, identifiable, compositional types: thus the structure of V_3O_5 may be regarded as having been derived from that of rutile, TiO_2, where, at regular (121) CS planes, edge-sharing of MO_6 octahedra in the unfaulted rutile has given way, as a result of a $\frac{1}{2}[0\bar{1}1]$ displacement vector, to face-sharing.

In 1973, Chisholm, using the ideas of Wadsley and others regarding CS planes, formulated a unifying account of the structures of the linked silicates in which the chain silicates, comprising the pyroxenes and amphiboles, were shown to be directly related to the sheet silicates, represented by talc and mica. Thus a pyroxene, in which there are single strands of linked SiO_4 tetrahedra, may be 'converted', at least in analogical structural terms, to an amphibole, in which there are linked double strands of tetrahedra, by introducing a particular type of CS

† A CS plane is characterized by the fact that a component of the displacement (or shear) vector is perpendicular to the fault plane – e.g. the fault plane may typically be (121), as occurs in oxygen-deficient rutile, with the displacement vector lying in $[0\bar{1}1]$.

plane recurrently on every other (020) plane (i.e. at every second chain) with a displacement vector of $(\frac{1}{2}b + \frac{1}{2}c)$. Chisholm (1975) also drew attention to the fact that, if a CS plane of this kind were introduced recurrently at every chain, the original pyroxene structure would then be converted into continuous Si_4O_{10} sheets, as in the talc and mica structures. Apart from providing a plausible basis for interpreting, in geochemical terms, the progression along ostensibly disparate silicate structures, an attractive feature of this formulation is that it naturally includes those situations in which planar faults occur within what would otherwise be a perfect structure, itself made up of a regular CS sequence. Faults of this kind, in which the regularity of CS planes is disrupted, are known as Wadsley defects. When they occur in amphiboles they could, for example, represent a band of triple-, quadruple-, quintuple-, etc., or even singly linked tetrahedra within the matrix of doubly linked tetrahedra.

Even before Chisholm's formulation, a useful, though possibly more complex, scheme was proposed by Thompson (1970, 1978), who argued that most amphiboles can be thought of as 1:1 mixtures of pyroxene and mica, sectored, so to speak, along the pyroxene *c*-glide planes and the mica *a*-glide planes into (010) slabs and hence reassembled. In a similar fashion other, intermediate chain silicates may be constituted, and it has recently been confirmed (Veblen *et al.* 1977; Jefferson *et al.* 1978) that chain silicate structures containing triple chains in ordered sequence do indeed exist.

This report represents part of a continuing high resolution electron microscopic study of minerals in general (Thomas 1974, 1977; Jefferson & Thomas 1974, 1975, 1977, 1978, 1979; Thomas & Jefferson 1978; Thomas *et al.* 1976; Evans *et al.* 1972; Evans & Thomas 1975). It was felt that there was especial merit in confining attention, in the first instance, to one type of amphibole. Ultimately it should prove feasible to explore variations in ultra-structure among specimens of the same mineral taken from different geological habitats. This approach should, *inter alia*, afford clues as to the variations in the coexistence of multiple-chain silicate structures. It should also reveal hitherto undiscovered topologies and structures of crystalline inorganic silicates.

Nephrite, one of the two principal members of the so-called jade minerals, is a tough, highly compacted and fine-grained form of the amphibole known as actinolite, with the general chemical formula $Ca_2(Mg,Fe)_5(Si_4O_{11})_2(OH)_2$. In the iron-free variety it possesses the composition of tremolite, $Ca_2Mg_5(Si_4O_{11})_2(OH)_2$, and is white in colour, but its appreciation over the centuries by many civilizations, especially that of China, comes from its wide variation in colour due to the presence of other cations, although the commonly observed green shade is thought to be due to the presence of iron. Dr A. C. Bishop and his colleagues at the British Museum kindly made available a wide range of specimens. Nephrite was selected because it had hitherto (Mallinson 1976; Hutchison *et al.* 1976; Mallinson *et al.* 1977; Jefferson *et al.* 1978) been shown to be stable in the electron beam and to be amenable to high resolution studies.

The most important feature of the structure of amphiboles is the presence of doubly linked silicate chains running parallel to [001]. These chains are separated laterally by cations in various sites. Nephrite is a monoclinic amphibole, with unit cell parameters: $a = 9.89$ Å, $b = 18.20$ Å, $c = 5.30$ Å, $\beta = 104.64°$; the structure belongs to the space group $C2/m$ (Mitchell *et al.* 1971). Figure 1 (*a* and *b*) shows the crystal structure in terms of coordination polyhedra from two different orientations.

The principal, long-term aims of this work are, first, to identify and characterize the nature of the faults that occur in amphibole minerals; second, to seek clues as to how triple-, quadruple-

and higher-order chains come to be accommodated within the parent matrix. (The existence of a triple chain in amphiboles was first established by Hutchison *et al.* 1975. It is also of interest to note that the infraction visible in figure 12(*a*) of the electron micrograph of tremolite published by Heide (1963) probably arose from an isolated multiple-chain fault in the amphibole.) Is there, for example, a gradient in substitutional impurity which is associated with such faults? Can new topologies, therefore, be fashioned by appropriate chemical doping?

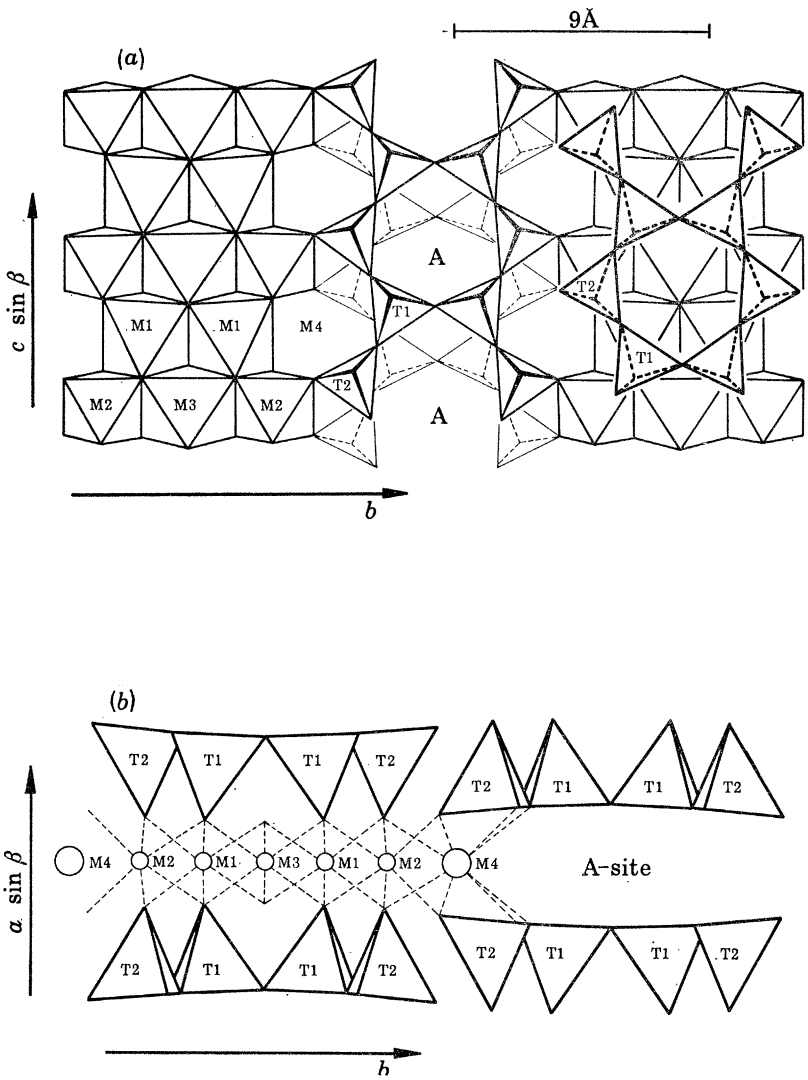

FIGURE 1. Polyhedral diagrams of the monoclinic amphibole structure. (*a*) Projection down the [100] axis (the axis of the electron microscope observations), showing the doubly-linked chains of silicate tetrahedra running parallel to the [001] axis. (*b*) Projection down the [001] axis, showing the various cation sites. Note how alternate double chains along [010] have their tetrahedra pointing in opposite directions.

Third, we wish to arrive at the mechanism of conversion from double chains to triple and other multiple chains, and also to understand other remarkable faults (see §4*c*) that can be incorporated apparently without strain by the amphibole structure. Only some of these long-term aims have so far been realized. Throughout most of this work we have used the high resolution electron microscopic approach that has proved so valuable for other minerals

(Jefferson & Thomas 1974, 1978; Jefferson *et al.* 1976; Buseck & Iijima 1974; Hutchison *et al.* 1975; Hutchison *et al.* 1977; Thomas & Jefferson 1978). As we shall demonstrate later, by comparing computed and observed images the trustworthiness of our results could be assessed. A brief account of part of this work was published earlier (Jefferson *et al.* 1978).

2. Experimental

Six specimens of nephrite were examined, their origin and British Museum catalogue numbers are: 26812–New Zealand; 1947, 325–Monterey Co., California; 1961, 404–Mashaba Chrome Mine, Victoria, Rhodesia; 1961, 127–Fraser River, British Columbia; 41830–South Sea Islands; 56284–Jordansmuhl, Breslau, Silesia.

For electron microscopic investigation, small fragments were removed from each specimen, embrittled by immersion in liquid nitrogen and crushed to a fine powder in a percussion mortar. A suspension of the powder in chloroform was then made by ultrasonic dispersion and a drop of the suspension placed on a copper grid, which had been precoated with a 'holey' carbon support film. Specimens prepared in this way yielded numerous small wedge-shaped crystals, with edges sufficiently thin to enable lattice images of reasonable contrast to be observed from crystals that lay over holes in the support film. All specimens were examined in a Siemens Elmiskop 102 electron microscope at an accelerating voltage of 100 kV, using a $\pm 45°$ double-tilt stage, with a z axis adjustment. Images were recorded at magnifications within the range $(2–5) \times 10^5$; an objective aperture of 40 μm diameter in the back focal plane of the objective lens permitted diffracted beams corresponding to d-spacings of 3.88 Å† and greater to contribute to the image.

Whenever possible, interesting regions of a particular crystal were examined in the microscope, after imaging, by energy dispersive X-ray analysis, with a view to detecting any change in composition arising from the incorporation of defects in an otherwise regular structure. The spatial resolution of these efforts was limited by the large probe size (between 1000 and 2000 Å in diameter) of the instrument used.

Selected micrographs, particularly those showing isolated or repeated defects, were subsequently examined by optical diffractometry (Millward & Thomas 1975) in an attempt to detect small changes in lattice geometry in matrix regions adjacent to structural defects. This technique, in which a portion of an electron micrograph is used as object for diffraction by laser light, is effectively capable of selecting any region of a crystal about 250 Å in diameter and is a particularly powerful method of detecting microstructural irregularities, subunit cell 'strain', or long period superlattices which are otherwise not readily perceived.

Crystals of clino-amphibole, of which nephrite is an example, usually lie with (100) planes parallel to the surface of the support film and some specimen tilting, principally around the [010] axis, is required to bring such crystals into an orientation suitable for producing a lattice image. A very slight tilt (*ca.* 1°), about this axis, of a crystal lying on (100), brings the electron beam parallel to [201], and the $(hk\overline{2h})$ reciprocal lattice section into the back focal plane of the objective; but under such conditions the objective aperture allows only $(0k0)$ diffracted beams to contribute to the final one-dimensional image. Two-dimensional lattice images, which yield much more information, can be obtained by tilting crystals by approximately 16° about [010] from their normal positions. In such cases the reciprocal lattice section $(0kl)$ or $(hk\bar{h})$ is brought

† 1 Å = 10^{-1} nm = 10^{-10} m.

into the back focal plane, with the beam parallel to [100] or [101] respectively. In practice the two sections can be distinguished owing to the systematic absences of the $C2/m$ space group, the $(0kl)$ section having maxima only with k even on all rows, whereas in the $(hk\bar{h})$ case k is odd or even on alternate rows (see Hutchison *et al.* (1976) for further details). The $(0kl)$ section was found to give the most suitable lattice images; the electron beam is parallel to the [100] axis of the amphibole structure and images could readily be interpreted in terms of the projected charge density (p.c.d.) approximation (Lynch *et al.* 1975). All the lattice images presented herein were recorded with this orientation.

3. Computation of images for ideal and faulted tremolite and actinolite

In parallel with the experimental work, theoretical electron microscopic image calculations were undertaken in order to determine the range of specimen thicknesses under which the p.c.d. approximation was valid for $(0kl)$ lattice images of nephrite, and hence the range within which intuitive interpretation of image contrast, particularly in regions involving defects, could be made. Images were calculated by using the multislice approximation (Cowley & Moodie 1957*a*), which has been fully described elsewhere (Lynch & O'Keefe 1972; Goodman & Moodie 1974; Anderson & Tilley 1974), but, in view of its importance, we will summarize the physical principles involved.

In principle, the multislice procedure copes with multiple scattering within a crystal by dividing the latter into slices of such thickness that *multiple* scattering within each slice can be neglected. The wave amplitude $\psi(x, y)$ scattered by each slice may then be represented by

$$\psi(x, y) = \exp\{i\sigma\phi(x, y)\}\Delta z, \tag{1}$$

where Δz is the slice thickness and σ an interaction parameter defined as

$$\sigma = \frac{2\pi}{\lambda E}\frac{1}{1+(1-v^2/c^2)^{\frac{1}{2}}}, \tag{2}$$

λ being the electron wavelength, E the accelerating voltage, v the electron velocity and c the velocity of light. The slices are represented by *planes*, separated by vacuum gaps, the emergent wave amplitude being calculated by allowing for successive interactions of the wavefront with each plane in turn, followed by propagation across the vacuum gap to the next slice and so on. Thus $\psi_1(x, y)$, the wave amplitude immediately following the first plane, after propagation across the gap to the next plane, will be of the form

$$\psi_1'(x, y) = \exp i\sigma\phi(x, y)\,\Delta z^* \exp(2\pi i/\lambda)\{(\Delta z^2+x^2+y^2)^{\frac{1}{2}}-\Delta z\}, \tag{3}$$

where * signifies convolution. After the second plane, the wavefront becomes

$$\psi_2(x, y) = \psi_1'(x, y)\exp\{i\sigma\phi(x, y)\}\Delta z. \tag{4}$$

Clearly, the wave amplitude, after the nth plane may be written in terms of that after the $(n-1)$th plane as

$$\psi_n(x, y) = [\psi_{n-1}(x, y)^* \exp(2\pi i/\lambda)\{(\Delta z^2+x^2+y^2)^{\frac{1}{2}}-\Delta z\}]\exp\{i\sigma\phi(x, y)\}\Delta z. \tag{5}$$

In this way the emergent wavefront can be written in terms of that incident on the first plane, the number of individual operations depending on the number of slices into which the crystal

is initially divided. Although it does not produce a suitable analytical output, the method is eminently suitable for the required computation and, once established, can be used as a routine technique for calculating the image features generated by an assumed structure. The method is not, unfortunately, invertible: consequently, calculations can be made only from proposed structural models. An observed image cannot lead us, by computational means, to the structure responsible.

For nephrite, the slice thickness – which is the quantity that is multiplied by the p.c.d. in the multislice method, was limited to 2.5 Å, emergent wave amplitudes being calculated for effective specimen thickness in the range 2.5–1000 Å. After modification by the phase-contrast transfer function (Erickson & Klug 1971) and aperture function, the amplitudes were Fourier-transformed to produce theoretical (0*kl*) images. Defect of focus was sampled at intervals of 100 Å in the region from 0 to −1600 Å, those in the region −800 to −1200 Å being particularly important for image interpretation in terms of projected structure, since, at these values of underfocus, approximately equal instrumental phase shifts occur in all the diffracted beams contributing to the image. Both the coefficient of spherical aberration (C_S) and the objective aperture radius in reciprocal space were dependent upon the focal length of the objective lens, which in turn varied with the specimen height. Images were calculated for a number of objective aperture radii, and it was found that this radius could not be decreased beyond 4.4 $Å^{-1}$ without significantly altering the image contrast due to the elimination of important diffracted beams. Trial calculations involving increases in objective lens spherical aberration and compensation for chromatic aberration (variations in accelerating voltage and lens currents frequently referred to as 'depth of focus') revealed that these factors had little effect upon image contrast with the aperture sizes employed. They were therefore neglected in subsequent calculations.

For the perfect structures, image calculation was relatively straightforward, but special conditions were needed in the calculation for isolated defects. As no digital calculation can be performed for an aperiodic object, the compromise procedure of Grinton & Cowley (1971) was employed. This involves placing the defect in the centre of an artificially large 'unit cell', surrounded by considerable areas of regular structure. The method, which has previously been used in similar problems (Jefferson *et al.* 1976; Spence 1976; Cowley 1977) is reliable only if the defect of focus is limited such that Fourier images (Cowley & Moodie 1957*b*; Rogers 1969) of adjacent cells do not superimpose to any great extent (i.e. the unit cell width must be sufficiently large) and if the crystal thickness is restricted such that the spreading wavefronts from adjacent cells do not interfere; for the range of defocus and thickness values used here, both conditions were satisfied. With the models of the faults described below, the defective structural band was bounded by two normal amphibole bands on one side and three on the other, giving rise to cell widths ranging from 50 to 73 Å. Subsequent calculations then involved 'multislicing' and transforming up to 287 beams, which could readily be handled by computer. All calculations were carried out on a CDC 7600 computer at the University of Manchester Regional Computer Centre.

4. Results

(*a*) *Experimental and calculated images of nephrite*

Calculated images of the perfect tremolite structure, $Ca_2Mg_5(Si_4O_{11})_2(OH)_2$, and an actinolite structure, $Ca_2(Mg, Fe)_5(Si_4O_{11})_2(OH)_2$, (based upon site occupancies as determined

by Mitchell *et al.* 1971) are shown in figure 2 (plate 1), for the optimum defocus (−1000 Å) and with a crystal thickness of 100 Å. The calculation simulated the inclusion of 19 beams within the objective aperture. The differences in contrast between the two images are negligible and thus enabled all subsequent image calculations to be made on the basis of the tremolite structure, obviating the need for allowance for ionic substitution, and greatly reducing the number of the input atomic parameters. Moreover, the similarity between the calculated images of tremolite and actinolite further implied that any substitution of cations on M1, M2 or M3 sites (see figure 1), such as could possibly occur in the vicinity of a planar fault, would not be detectable in the image contrast.

When evaluated for gradually increasing crystal thickness, calculations indicated that only slight variations in image contrast became evident up to a thickness of 400 Å. At greater thicknesses, however, changes in contrast became more marked. Figure 3 (plate 2) shows a series of images calculated at thicknesses from 2.5 to 1000 Å. Figure 4 (plate 1) is a defocus series from 0 to −1600 Å, at a crystal thickness of 100 Å. At this thickness the image can be interpreted, in terms of the crystal structure, within the region from 900 to 1100 Å underfocus. Figure 3 shows how the optimum defocus shifts slightly to higher values with increasing crystal thickness.

A detailed examination of the tremolite image in figure 2 reveals that, within the amphibole unit cell, four rows of white dots can be discerned, these being divided into pairs and referred to on the computed image as M or N dots respectively. The two sets reflect the fact that, in projection down the [100] axis, the two halves of the amphibole unit cell are identical. The more pronounced, M designated, set corresponds to the positions of the so-called A sites within the structure (figure 1); the positions of these dots were unaffected by increasing crystal thickness up to 400 Å. The A sites are unoccupied in tremolites and actinolites and, so far as the M dots are concerned, the p.c.d. approximation is clearly valid within this range of specimen thickness, since the A sites correspond to the regions of minimum projected charge density within the amphibole unit cell. The amphibole double chain, then, straddles the rows of M dots on (010). The intermediate, or N dots, which line the double-chain edges, serve to indicate the dangers of a naïve or literal application of the p.c.d. treatment. Their positions and intensities proved to be much more sensitive to thickness and defocus variations (see figure 3), while experimentally these variations were much larger; frequently these 'dots' were almost absent. Trial calculations simulating the effect of chromatic aberration and tests with larger coefficients of spherical aberration, together with variations in objective aperture size (i.e. limiting the resolution) failed fully to explain this behaviour. We believe that the variations in position and intensity of the N dots, as experimentally observed in the microscope, are due in large measure to slight tilts of the specimen away from the [100] zone axis. Changes in the orientation of a particular crystal, as detected by examination of the diffraction pattern, during study in the electron microscope are frequently observed; doubtless they arise from specimen heating which causes the crystal to bend locally and the stage to drift.

Taking due cognisance of the above factors, an intuitive interpretation of the contrast in the experimentally observed images proved possible. The principal features in observed image contrast were the M dots, and the presence, or otherwise, of the secondary N dots was unimportant. These conditions applied equally to images of defects, in addition to those of the perfect structure. A good example of one of the best experimentally observed images is shown in figure 5, (plates 3 and 4), together with an example of a (0*kl*) diffraction pattern from a well-

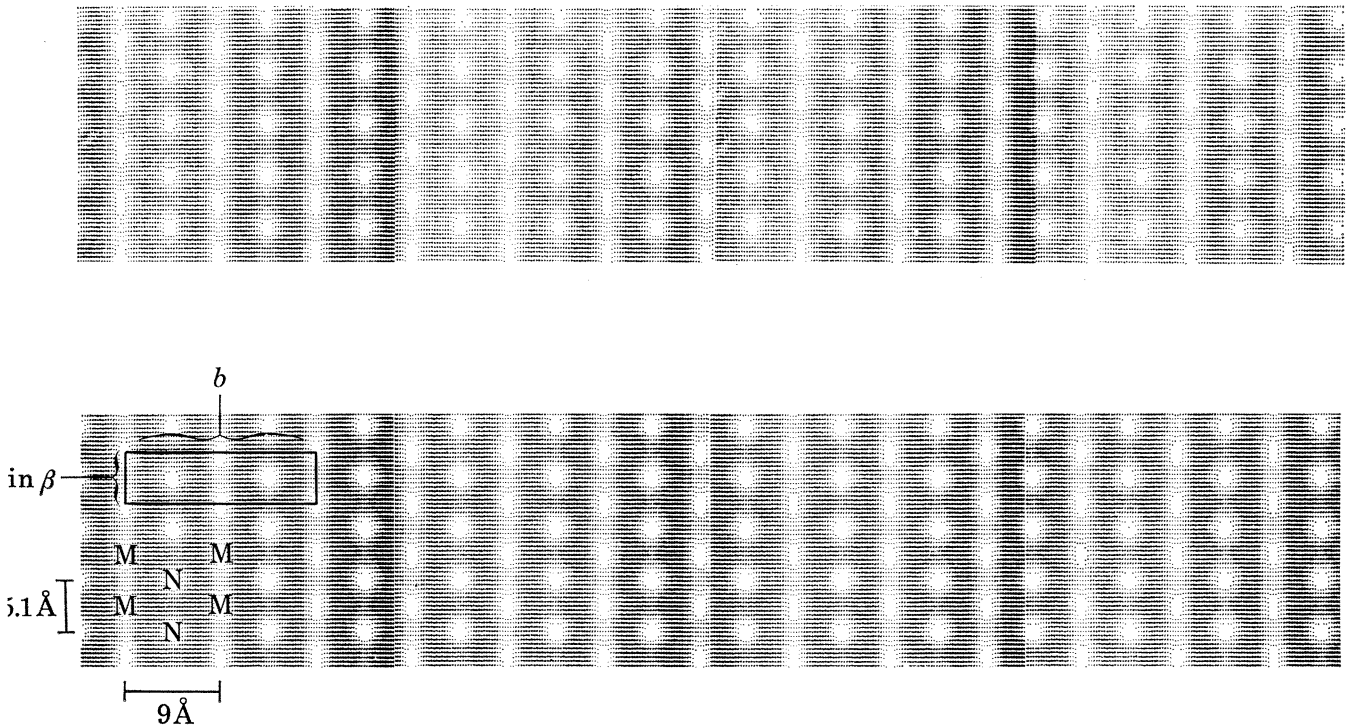

FIGURE 2. Computed, (0*kl*) electron microscope images of actinolite (*a*) and tremolite (*b*), for a crystal 100 Å thick and a defocus of 1000 Å. The notation used to describe image features in the text is indicated. (Non-uniformity of intensity in some areas is entirely due to line-printer faults and does not represent real variation.)

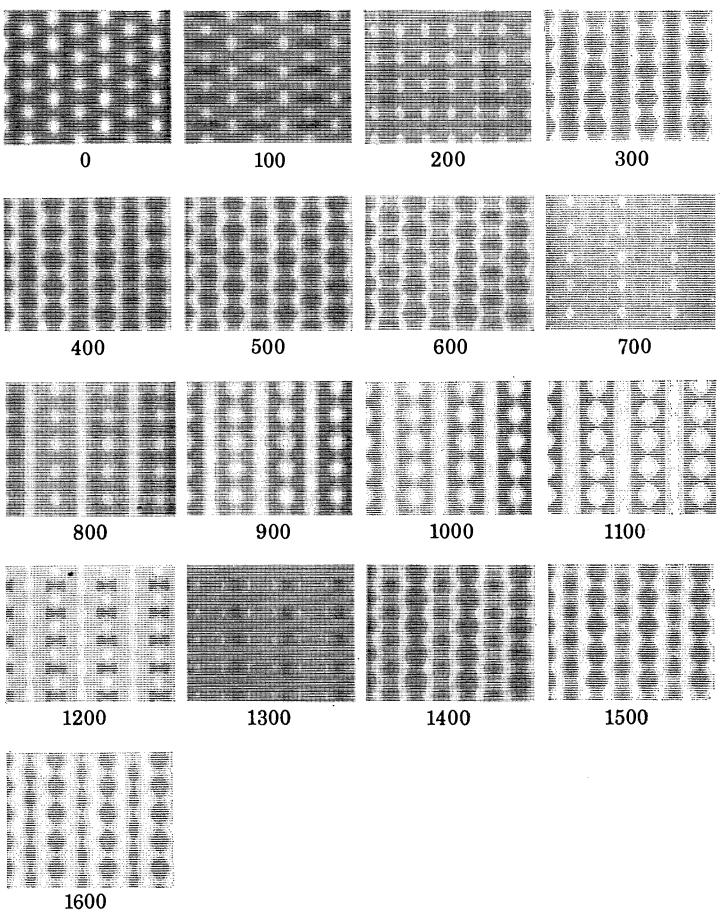

FIGURE 4. Computed images of tremolite, projected down [100], with defocus values from 0 to 1600 Å, for a crystal 100 Å thick. The image can be interpreted directly in terms of the crystal structure at defocus values around 1000 Å.

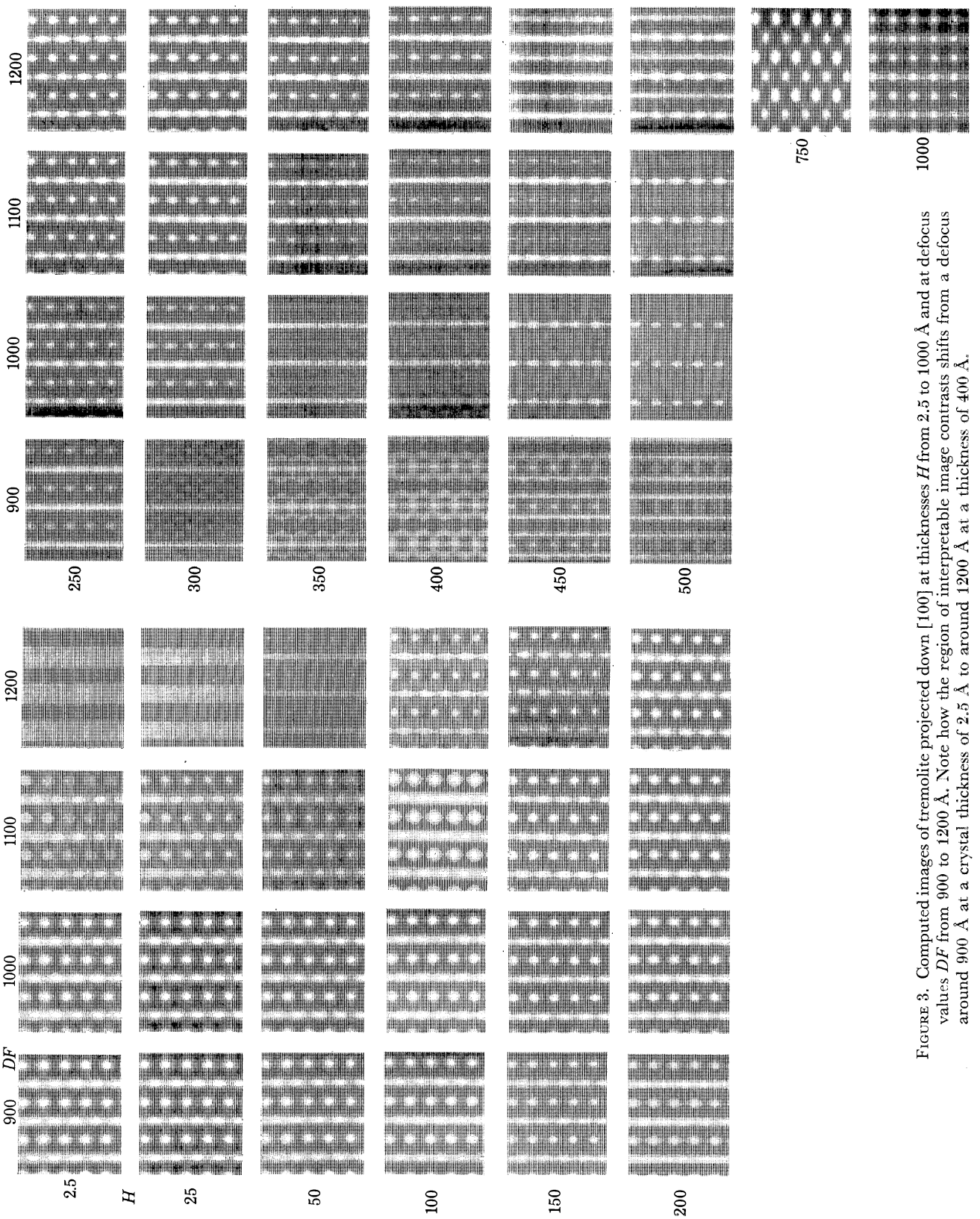

FIGURE 3. Computed images of tremolite projected down [100] at thicknesses H from 2.5 to 1000 Å and at defocus values DF from 900 to 1200 Å. Note how the region of interpretable image contrasts shifts from a defocus around 900 Å at a crystal thickness of 2.5 Å to around 1200 Å at a thickness of 400 Å.

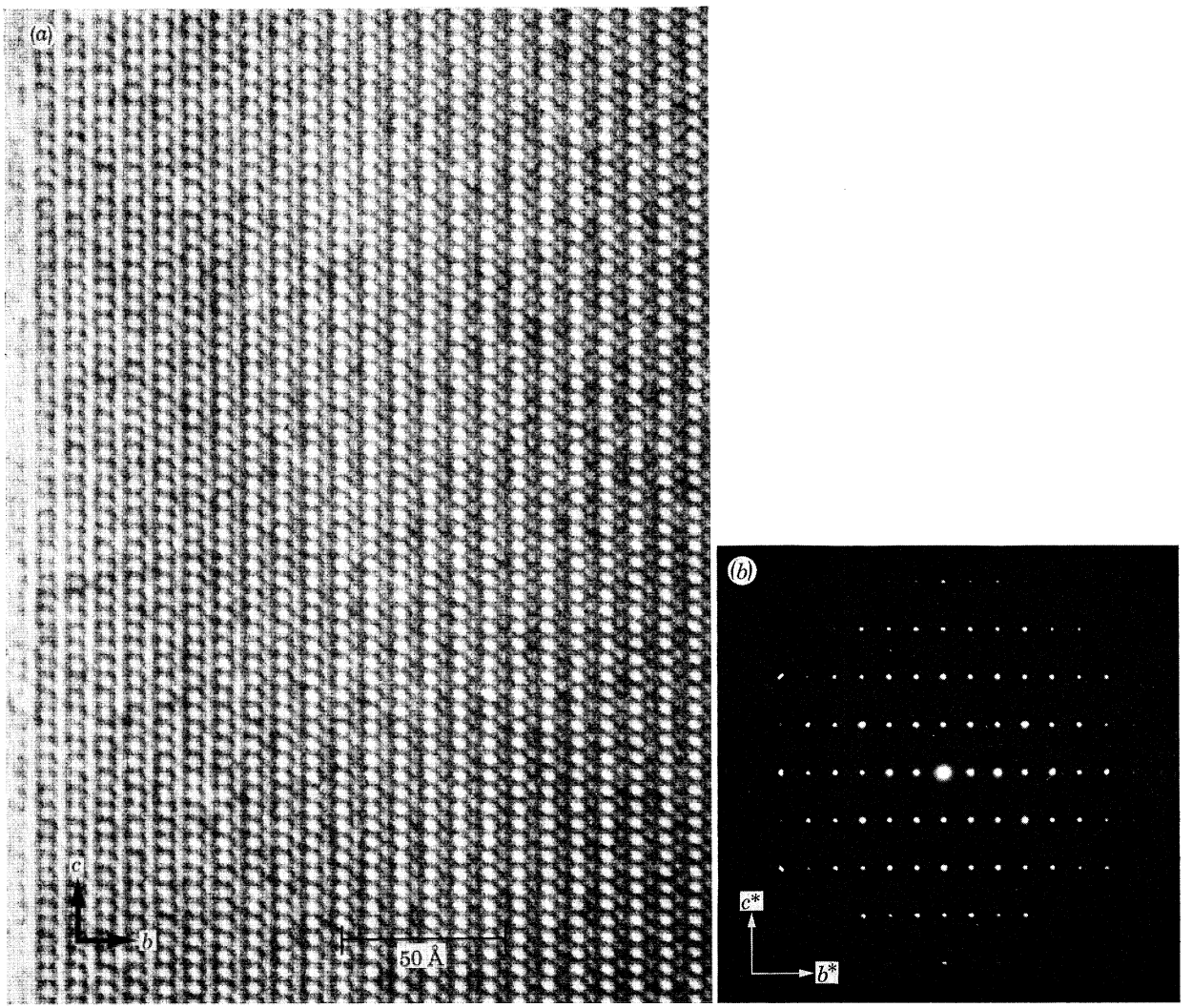

FIGURE 5. (*a*) Structural image from a portion of a crystal of Silesian nephrite, with the electron beam parallel to [100]. The crystal increases sharply in thickness from the edge, at the left, where the image matches those computed at thicknesses up to 500 Å, while towards the right-hand side the contrast closely resembles that computed for 750 Å thick crystals (see figure 3). (*b*) A (0*kl*) electron diffraction pattern from a nephrite crystal orientated precisely so that the beam is parallel to the [100] axis of the crystal.

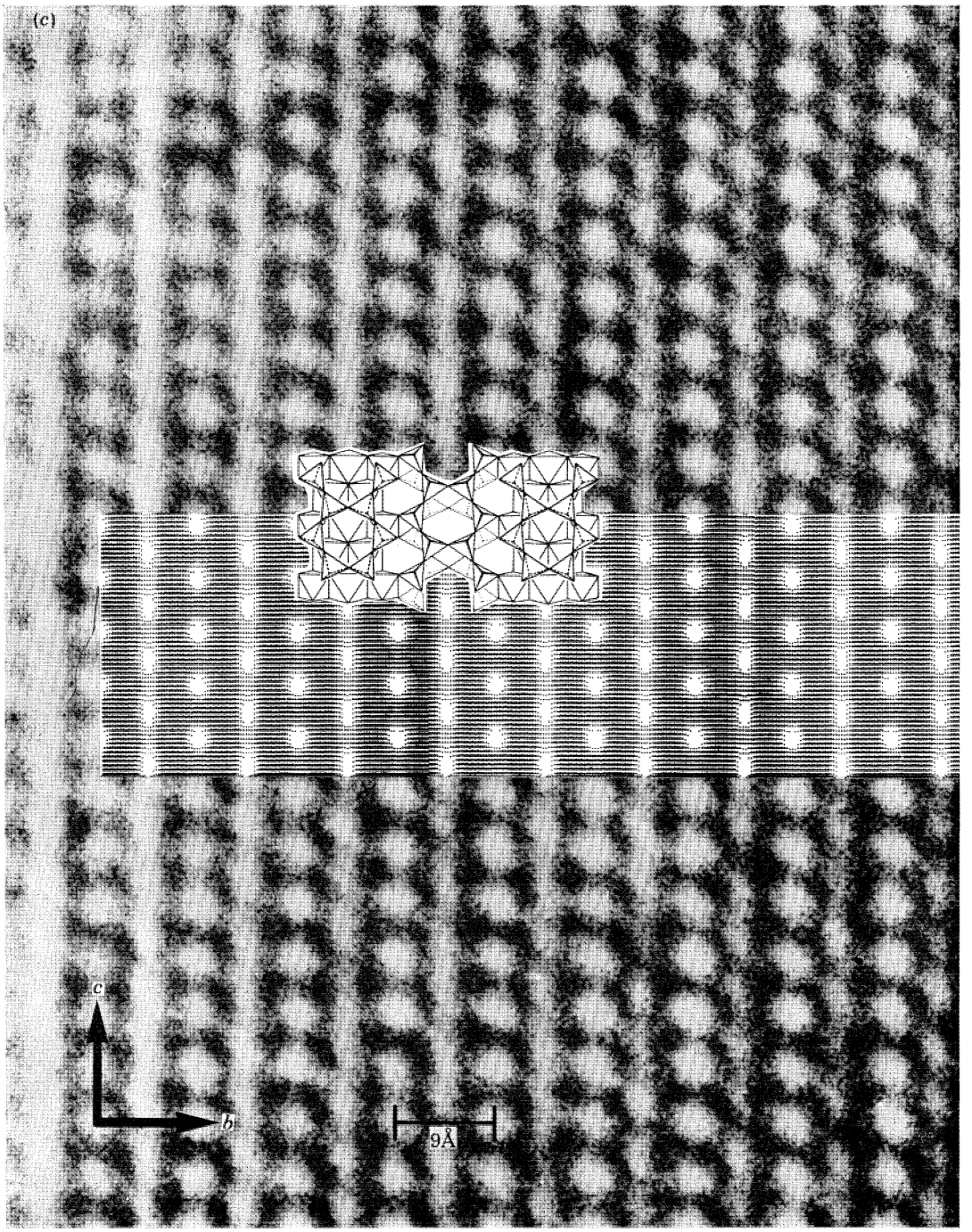

FIGURE 5. (*c*) A section of the image in (*a*) enlarged to show the match with a calculated image (for a crystal 100 Å thick and at a defocus of 1000 Å) and the amphibole structure.

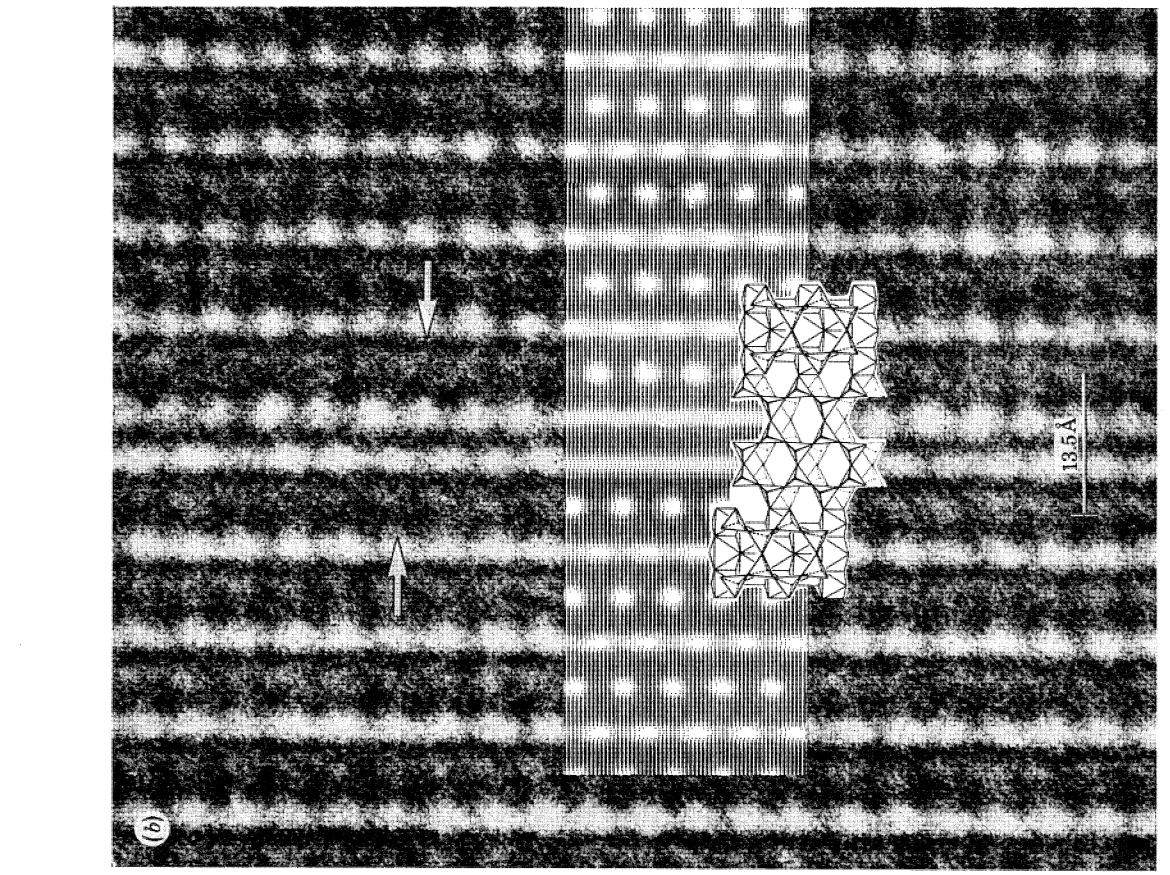

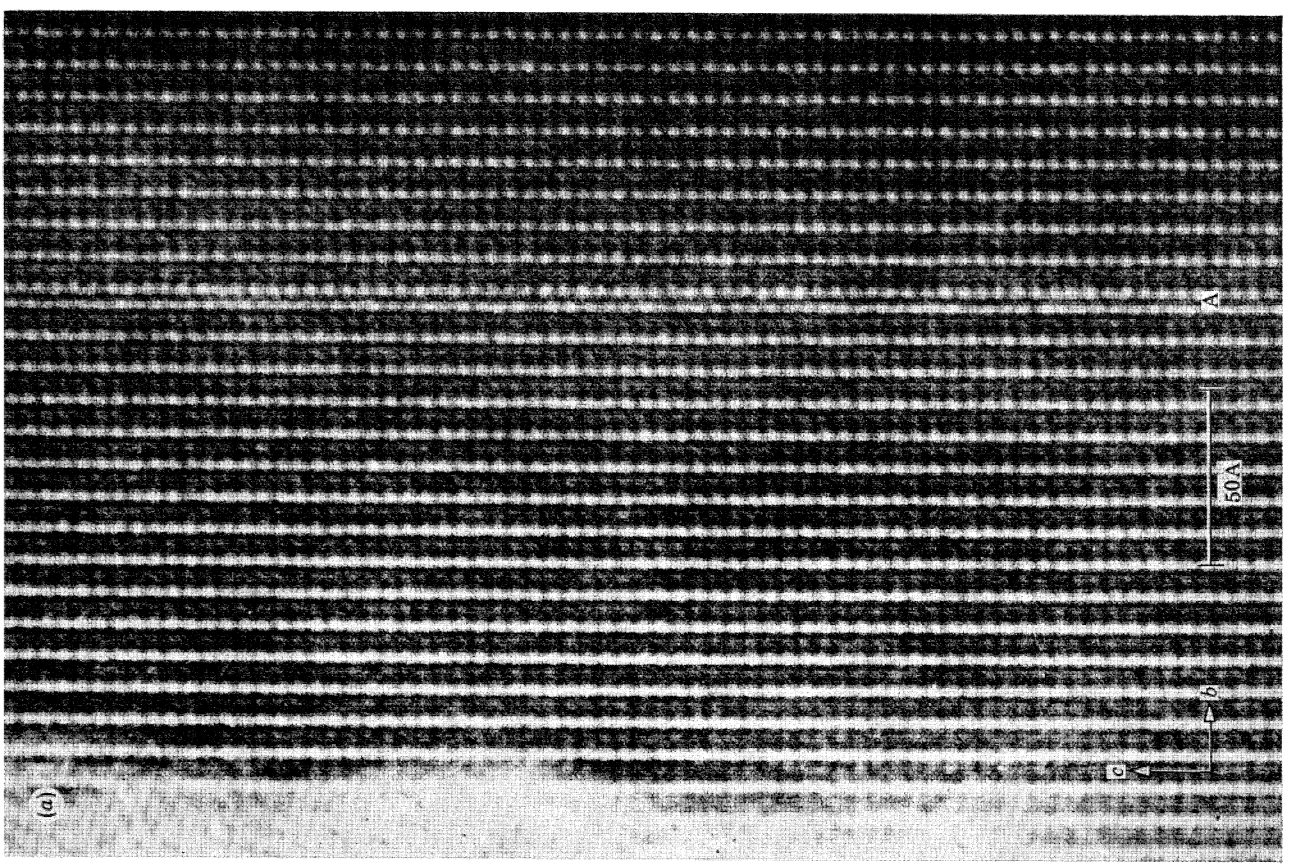

FIGURE 6. (*a*) A triple-chain defect at A near the edge of a crystal of nephrite from Rhodesia. (*b*) A portion of (*a*) matched with a computed image (thickness 100 Å, defocus 1000 Å) and the proposed defect structure. The antiphase of the (001) fringes across the fault is indicated by the arrows.

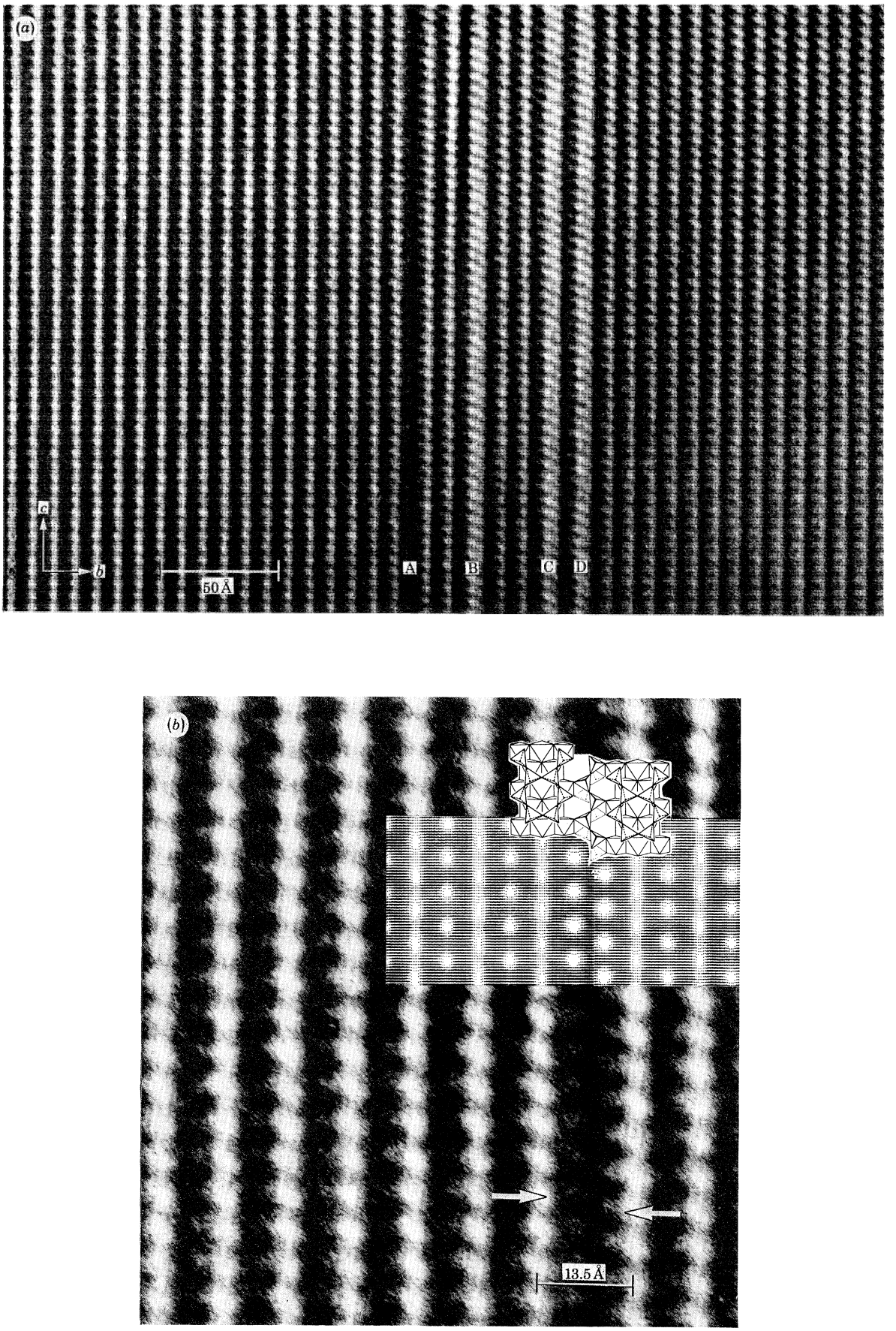

FIGURE 7. (*a*) A single chain present (in Rhodesian nephrite) in the double-chain matrix at A can be compared with three triple chains at B, C and D. (*b*) An enlargement of (*a*) shows the matching with an image computed for a single chain defect (100 Å thick, defocus 1000 Å), together with the structural interpretation on the same scale.

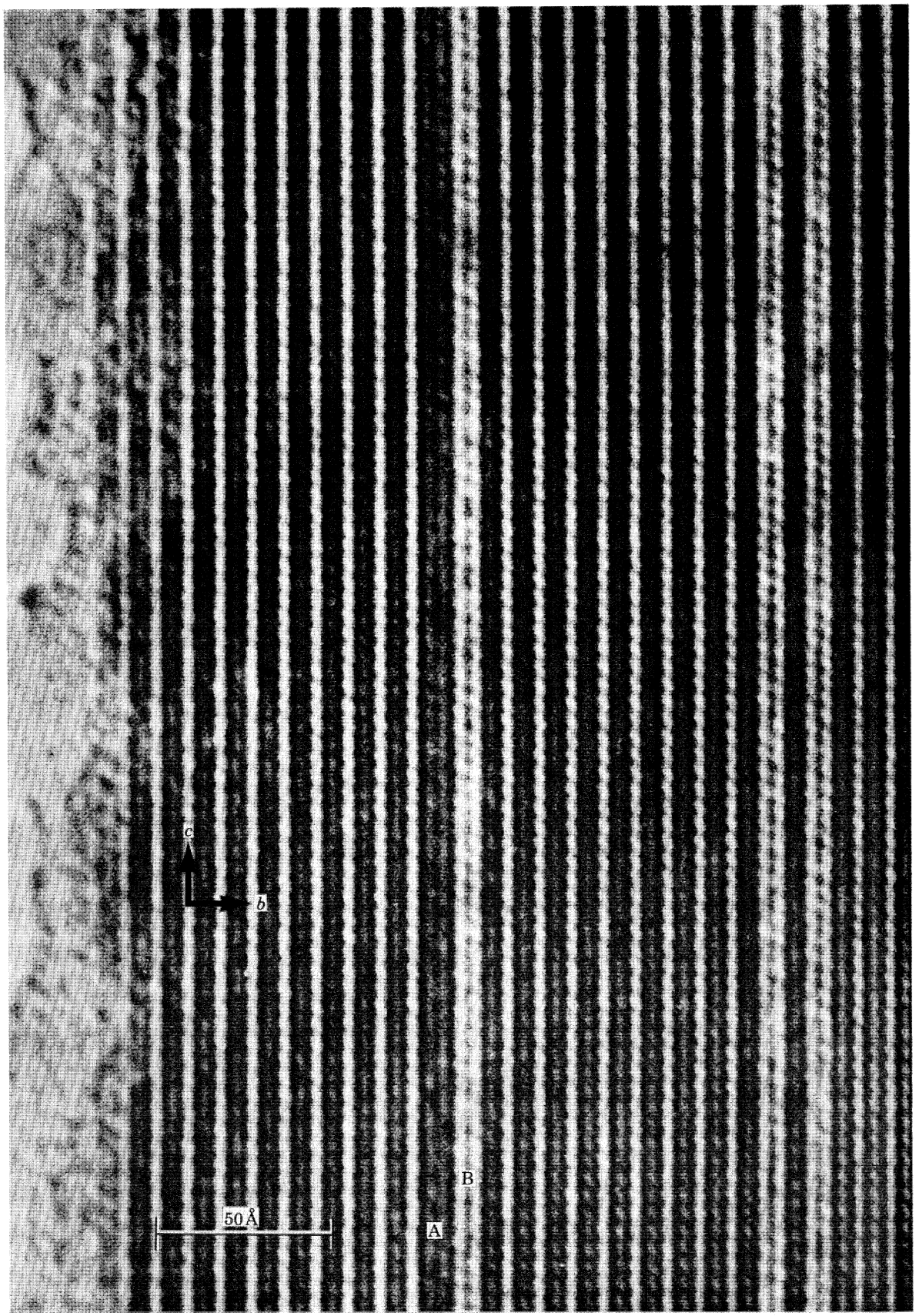

FIGURE 8. Rhodesian nephrite with a single chain (A) and a triple chain (B) occurring side by side in the amphibole matrix. Two adjacent triple chains can also be seen on the right.

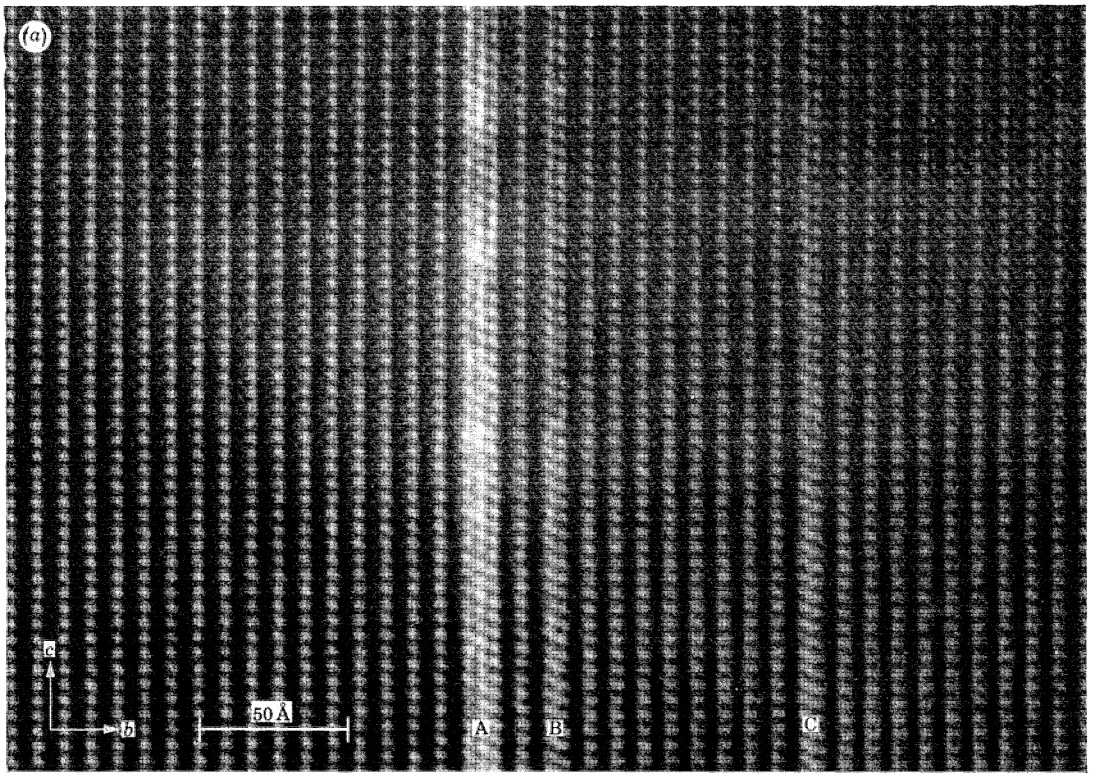

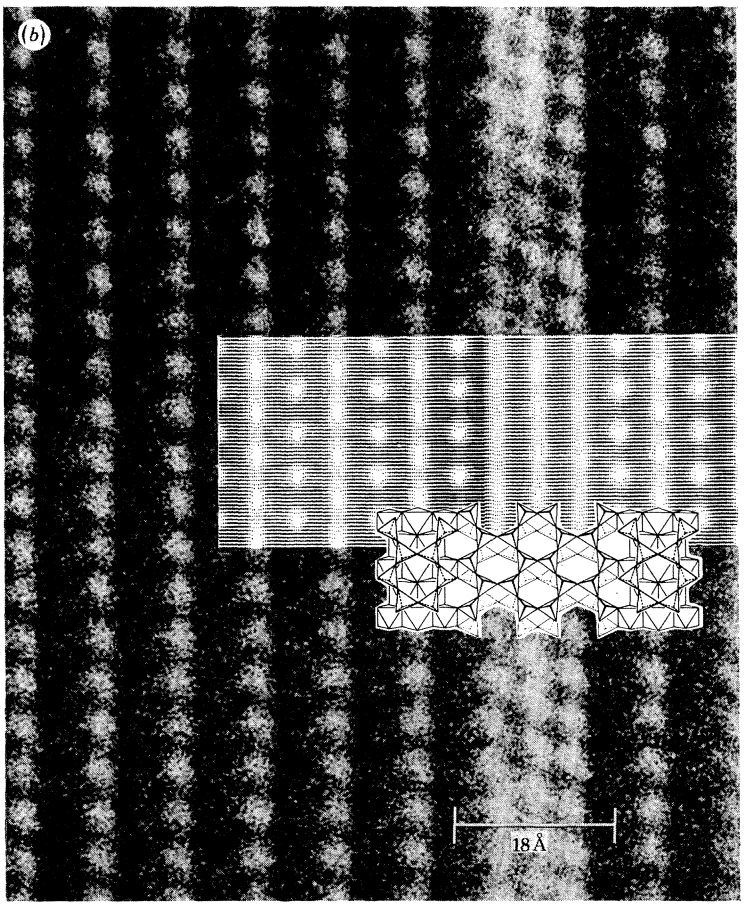

FIGURE 9. (*a*) Rhodesian nephrite with a quadruple chain defect at A, together with two triple chains, B and C, intergrown with amphibole. (*b*) An enlargement of A is compared with an image computed for a quadruple chain fault (thickness 100 Å, defocus 1000 Å), together with the proposed structure on the same scale.

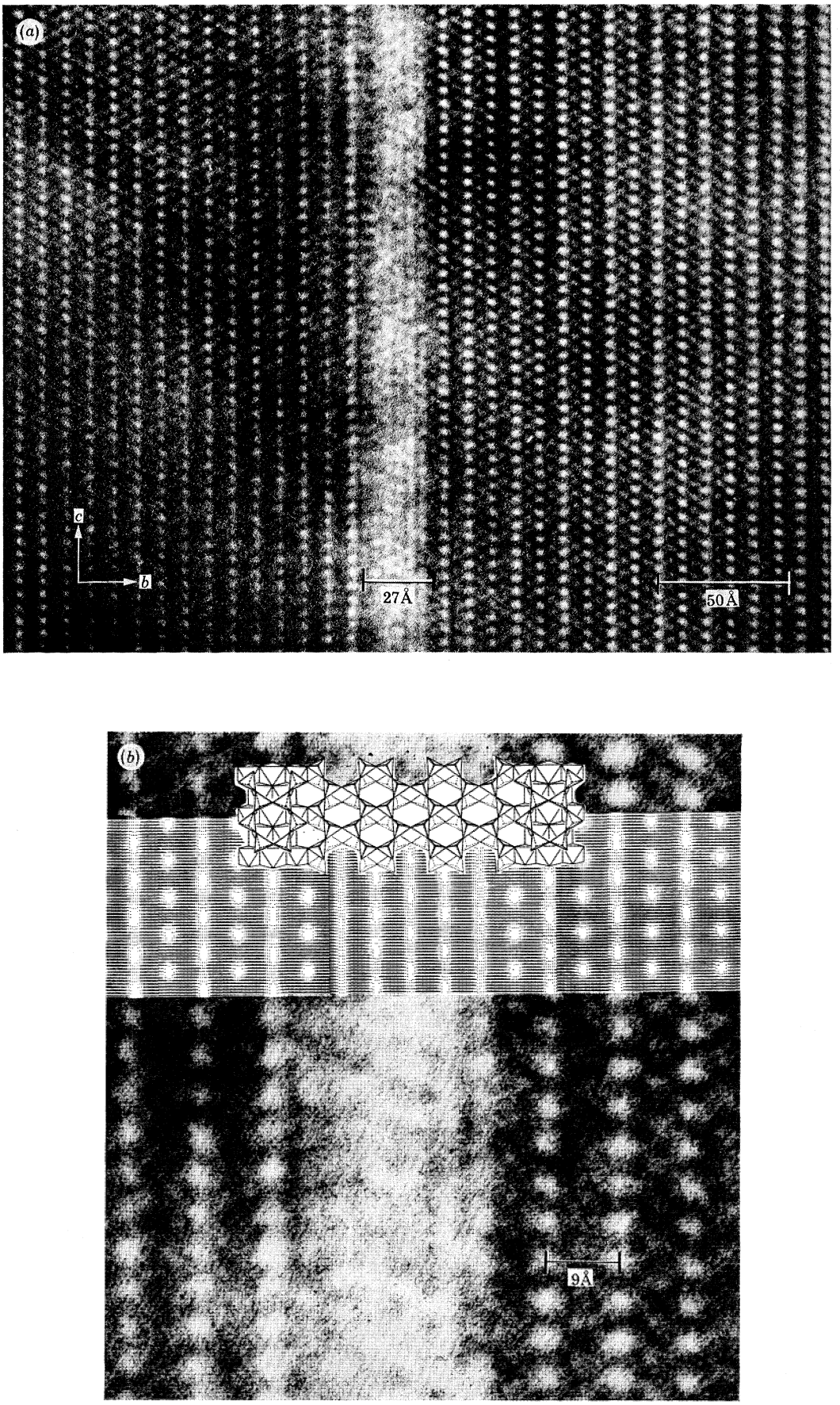

FIGURE 10. (*a*) A sextuple chain defect in New Zealand nephrite. (*b*) An enlargement of (*a*) showing matching with a computed image (thickness 100 Å, defocus 1000 Å) and the proposed structure. Note the tendency of the fault to suffer greater beam damage than the surrounding matrix.

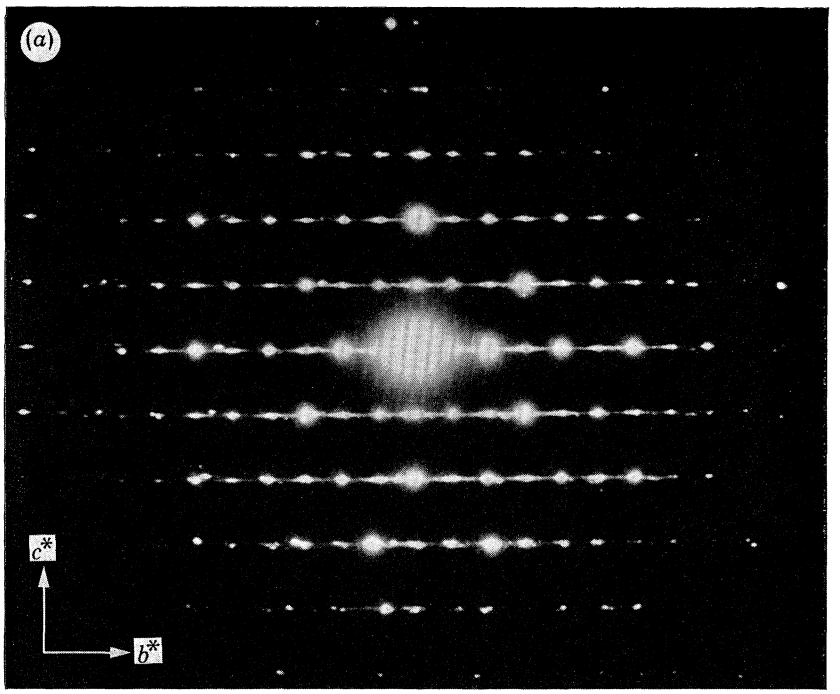

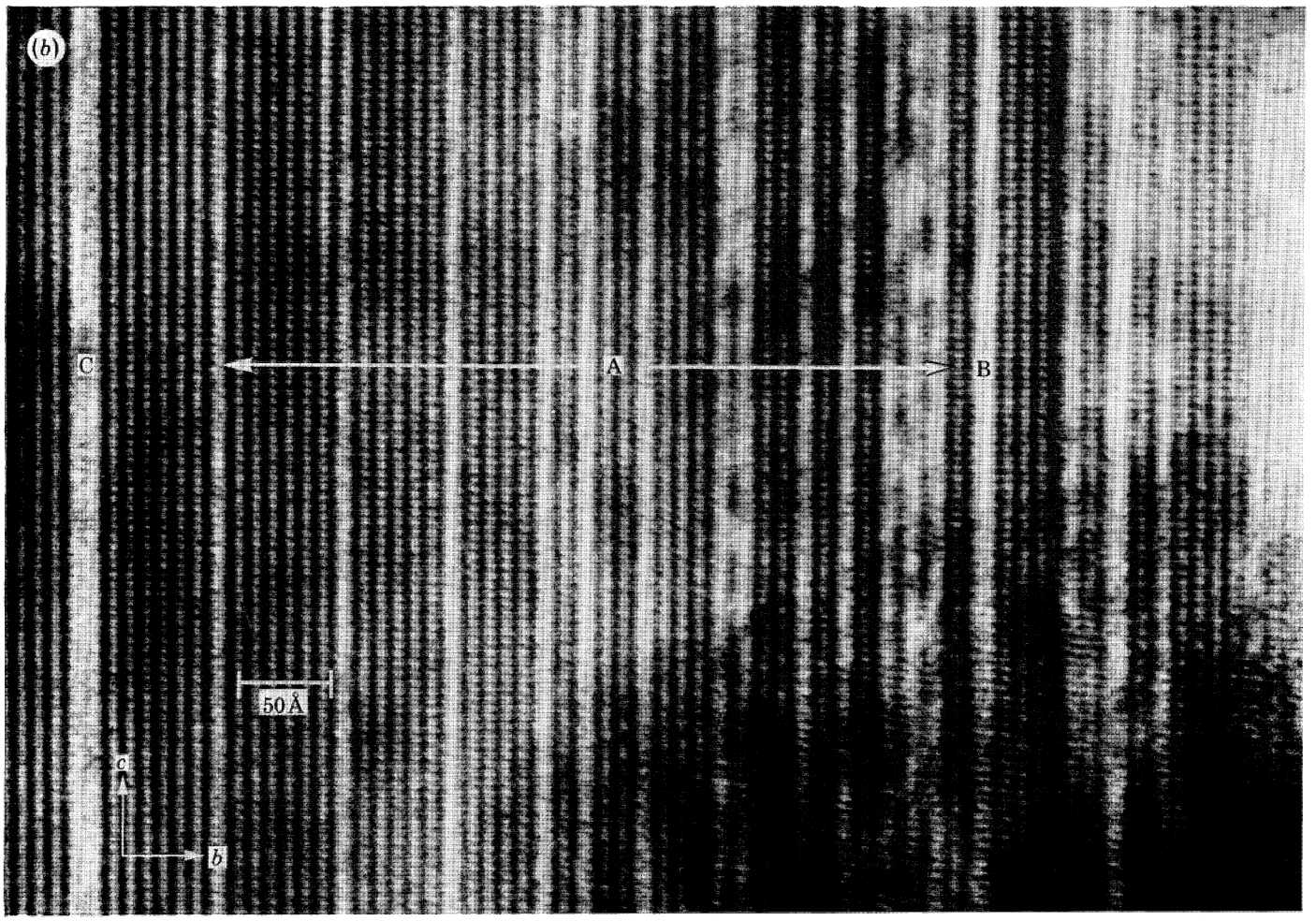

FIGURE 11. (*a*) A (0*kl*) electron diffraction pattern from a crystal of Rhodesian nephrite, showing extensive streaking along lines parallel to *b**. (*b*) The high degree of disorder indicated in (*a*) is manifest in the lattice image which shows an array of triple chains (A), a quadruple chain (B), and a possible quintuple chain (C).

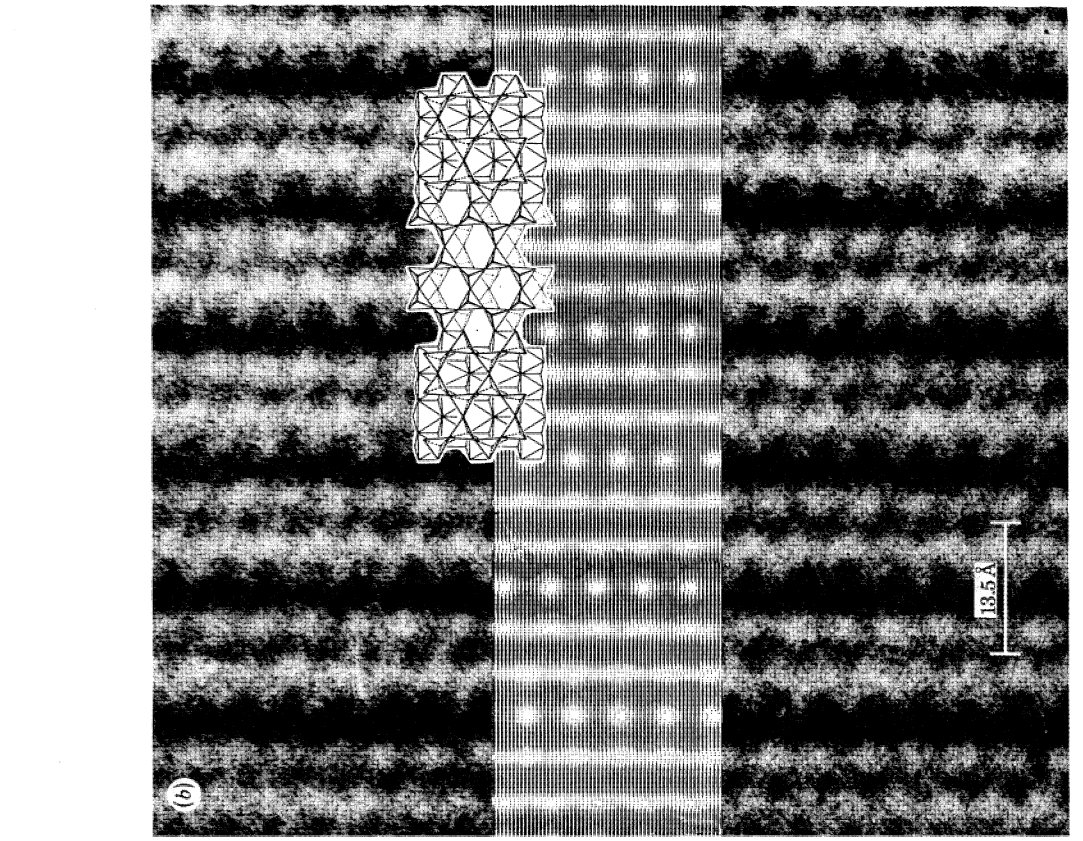

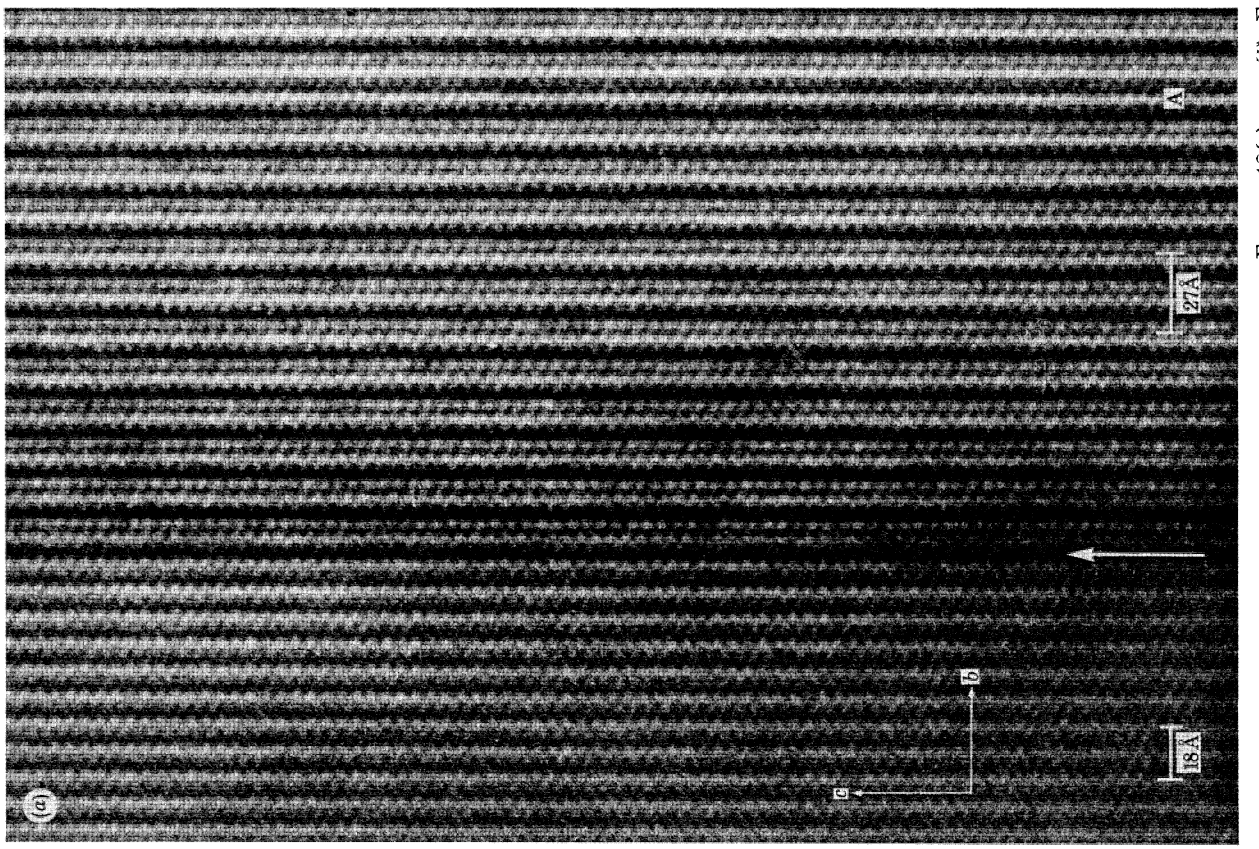

FIGURE 12(*a*) AND (*b*). For description see following page.

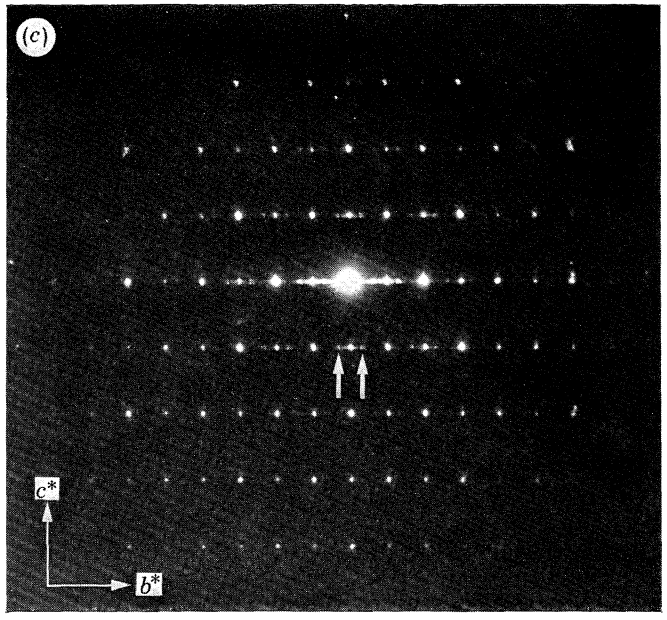

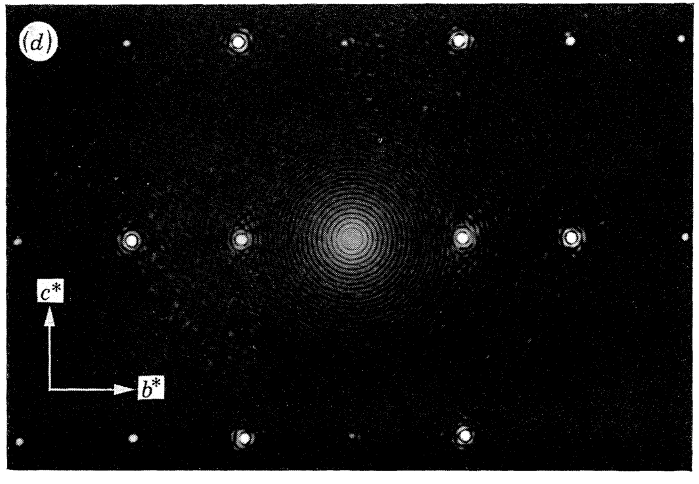

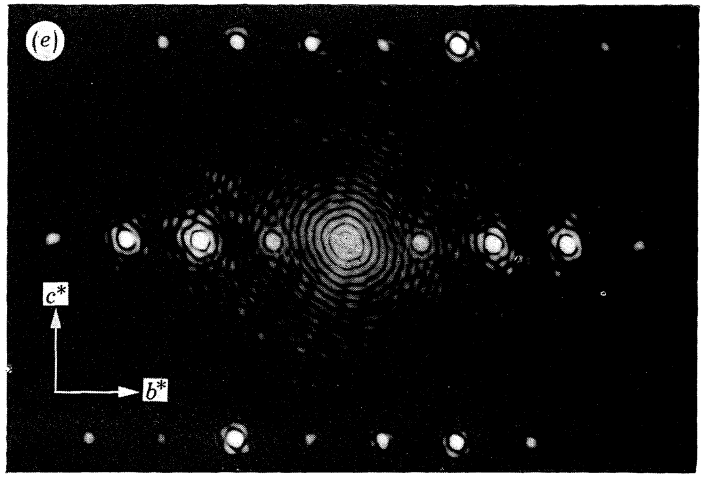

FIGURE 12. (*a*) Image from a crystal of Rhodesian nephrite showing an intergrowth of amphibole (on the left) with a structure comprising regular triple chains (on the right). A is a double-chain 'fault'. (*b*) An enlargement of (*a*) showing the match with a computed image (thickness 100 Å, defocus 1000 Å) and the proposed triple-chain structure. (*c*) A (0*kl*) electron diffraction pattern from the nephrite crystal incorporating the regular triple chains, containing extra reflections (arrowed) from the new structure. (*d*) An optical diffraction pattern from the left-hand side of (*a*) shows the

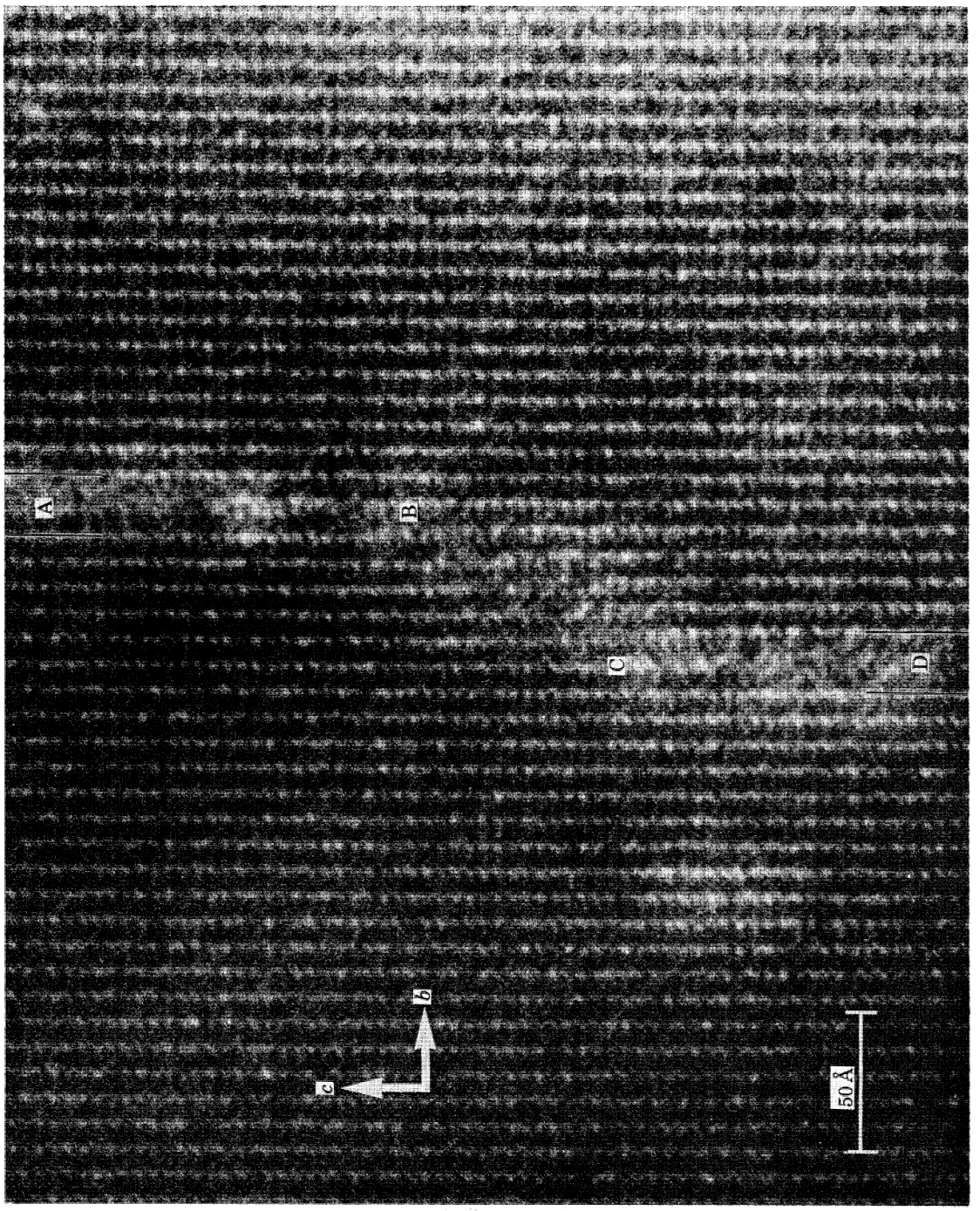

FIGURE 13. A triple-chain defect A–B, in a crystal of Californian nephrite, alters position in the crystal to C–D. The (020) fringes across the region B–C are in antiphase, best seen by viewing along DA.

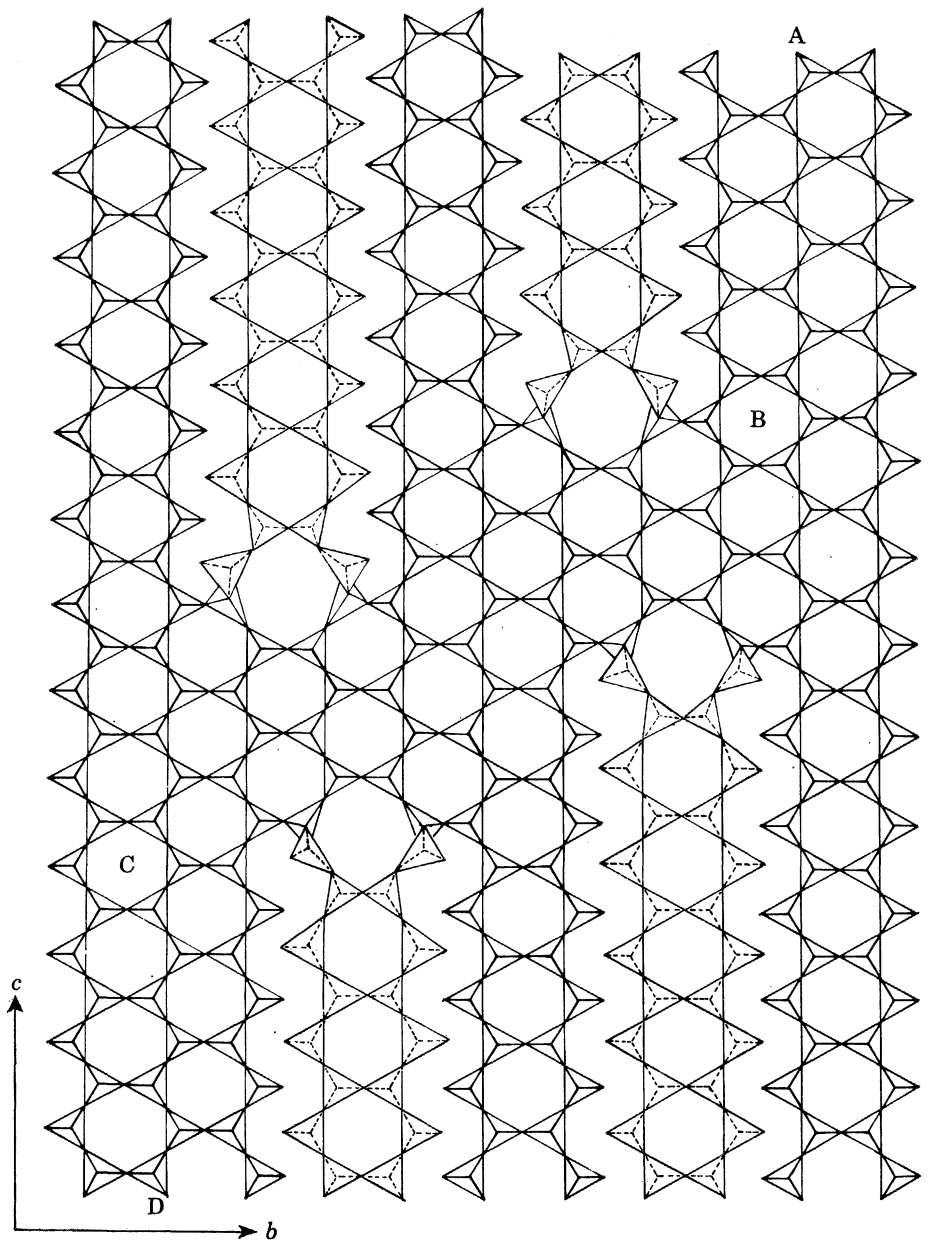

FIGURE 14. A possible structural interpretation of the phenomenon shown in figure 13. A triple chain A–B progresses through the crystal by means of a multiply-linked chain structure B–C which terminates in a triple chain C–D. Alternate amphibole double chains across BC share tetrahedral edges with the multiple-chain structure.

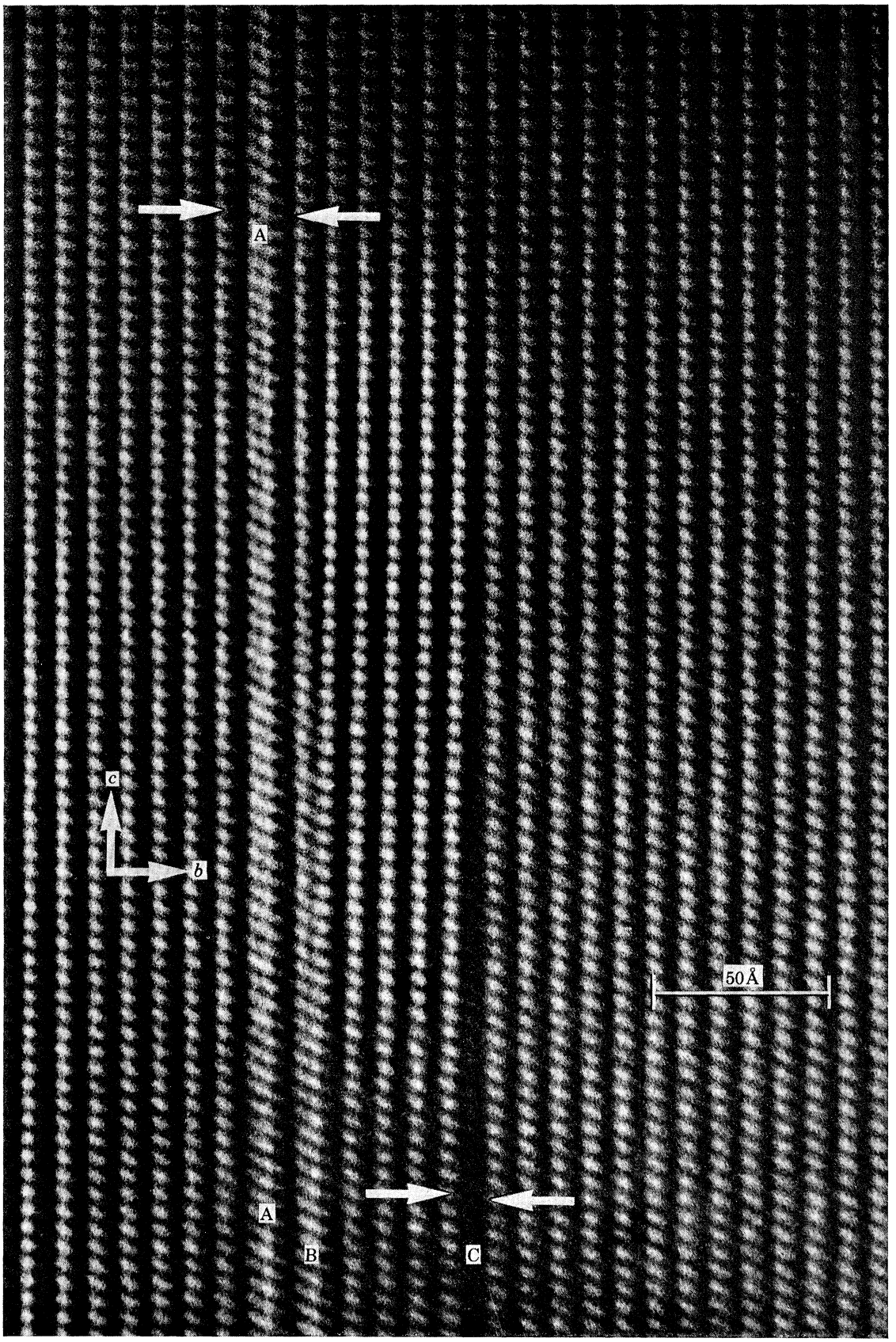

FIGURE 15. Two associated defect terminations in a nephrite crystal from the Rhodesian sample. Triple chain B and single chain C in the lower half are eliminated in the middle region and are not present in the upper half. The (020) fringes in the region between the two gradual terminations are bent and the contrast enhanced.

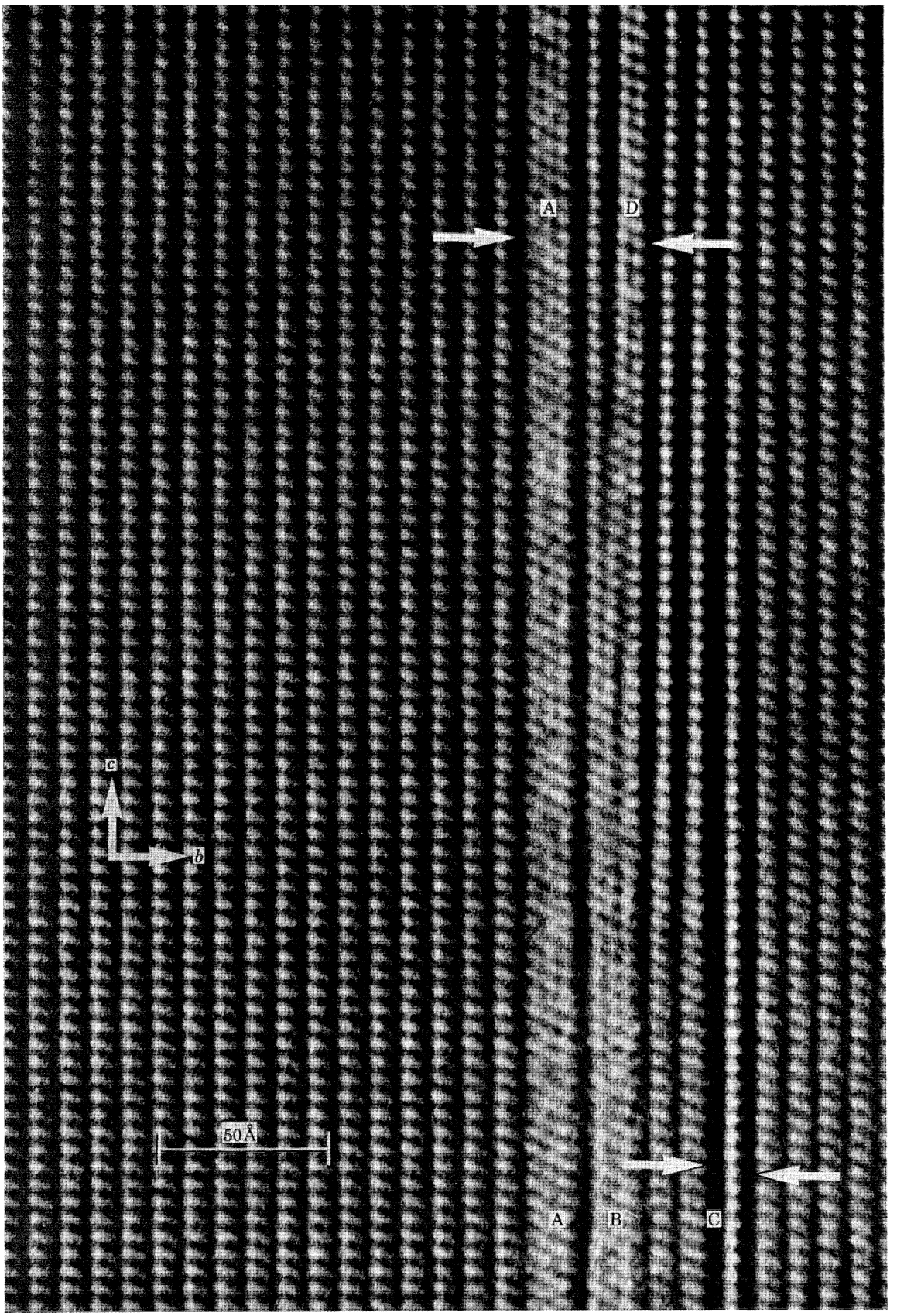

FIGURE 18. Another type of fault termination in Rhodesian nephrite. Two quadruple chains A and B and a single chain C are present in the lower half of the micrograph. Towards the upper half B is transformed into a triple chain D and C is eliminated. The region between the terminations shows fringe bending and anomalous contrast.

orientated nephrite crystal. The matching of the observed image, computed image and structural plan is also shown.

(*b*) *Computed images of defect structures*

In addition to image computations for the perfect structures, calculations were carried out for several distinct types of planar faults. The selection of these types arose directly from the images discovered by electron microscopy (see §4*c*). Images of single, triple, quadruple, quintuple and sextuple chain faults were simulated, while a trial calculation with a defect of six single chains, in effect a strip of pyroxene, was also carried out. As with the perfect structure, computed images of defects from the various models showed little change as the specimen thickness was increased to 400 Å, with the set of M dots corresponding nicely to the A sites within the faults. These image simulations are compared directly with experimental images in figures 6–10, with the relevant discussion in §4*c*. The N dot contrast (§4*a*) in particular provides the key to the interpretation. If the N dots are absent or nearly so in the image of the amphibole, then it is reasonable to expect that they be absent also within the defect part of the image. Defects containing only single chains, and therefore no A sites, should show only N dot contrast, and therefore dark contrast if the usual situation prevails where the N dots lack bright intensity. By comparison, multiple chain defects should exhibit only M dots and therefore bright contrast.

Calculations on faulted structures were confined to planar imperfections running throughout the crystal; the complexities of computing images of faults that terminate within the crystal (see figures 15–17 below) would be such as to demand excessive computer time. However, the applicability of the intuitive interpretation of the planar faults, as indicated by image calculation, augured well for its extension to more complicated defect phenomena.

(*c*) *Characterization of planar defect structures on* (010)

A variety of planar defects was observed, notably in the specimen from Rhodesia. They differed in width, but were of two general kinds: those that imposed an antiphase relation on the host structure along [001] and those across which the host structure remained in phase. In a previous paper (Hutchison *et al.* 1976) we argued that the former of these two types were lamellae in which the silicate chains were $(2n-1)$ tetrahedra wide and the latter chains of $2n$ tetrahedra width. Further examples and computer simulated images described below now permit us to identify such features unambiguously.

(i) *Triple-chain defects*

The most commonly observed type of (010) planar defect, found in all of our nephrite specimens, is one in which a double row of M dots, separated by *ca.* 4.5 Å, is evident and which produces an antiphase of the surrounding structure along [001]. A good example is shown in figure 6 (plate 5). A computed image based upon the structure plan shown is also included and, bearing in mind the comments about computed fringe image contrast made earlier, the agreement is good. The structure diagram shows how a lamella of a triple silicate chain inserted into the double-chain matrix fits the (010) fringe contrast and necessarily causes an antiphase of the host structure across the defect. The computed image was calculated for a crystal 100 Å in thickness and at an underfocus of 1000 Å.

(ii) *Single-chain defects*

As explained in §4*a*, the centre of an amphibole (double) chain is imaged as a row of white so-called M dots (see figure 2). The absence of a row of these dots, as at A in figure 7 (plate 6), together with an increase in the spacing between surrounding (020) fringes of one half of the double-chain width (4.5 Å) and the resulting antiphase of the (001) fringes, indicates that a lamella of pyroxene-like structure – a single chain – is present in the amphibole matrix. For direct comparison, within the same field of view are three triple-chain faults, two of which occur contiguously. Figure 7*b* shows a structural plan and computed image of this defect.

Figure 8 (plate 7) illustrates a rather unusual feature: a triple chain and a single chain that occur side by side, reflecting opposing chemical fluctuations. The presence of a triple chain implies a dilution of the calcium content of the crystal – the calcium ions line the edges of the chains in M4 sites (see figure 1) and are sited further apart by a multichain fault – whereas a single chain concentrates the calcium ions by bringing them closer together. Similarly a multiple chain will increase and a single chain will decrease the Mg, Fe content of the crystal (sites M1, M2 and M3.)

(iii) *Quadruple-chain defects*

The high resolution images presented so far show faults containing an odd number of silicate chains, setting the host structure in antiphase. Even-chain defects do, however, occur, producing no such antiphase. Figure 9 (plate 8) reveals a good example of a fault to which we can assign a quadruple-chain structure, together with a structural plan and computed image. A triple row of M dots characterizes such a defect.

(iv) *Quintuple-chain defects*

A fault containing five linked silicate chains would be characterized by four M-type fringes, an antiphase relation surrounding (001) fringes and a width of about 23 Å. A tentative example is shown in figure 11 (plate 10) at C, in a crystal exhibiting heavy faulting. See also §vi below.

(v) *Sextuple-chain defects*

Higher order chains than quadruple have been observed very rarely in nephrite specimens. One example of a sextuple chain fault in New Zealand nephrite is presented in figure 10, (plate 9) together with the structural interpretation and computed image.

(vi) *Extensive disorder*

Nephrite (0*kl*) diffraction patterns can display a remarkably high degree of disorder as evidenced by streaking parallel to b^*, as in figure 11*a*. The corresponding lattice image, shown in figure 11*b*, contains an irregular array of triple (A), quadruple (B) and possible quintuple (C) chain lamellae. Again we note the preponderance of triple-chain faults, which often occur together. Indeed, in figure 11*b* there is a suggestion that an ordered 'phase', composed of a sequence of six double chains and a triple chain, exists in coherent contact with the remainder of the crystal.

With increasing chain width the structure of a defect approaches that of the sheet silicate talc and, as the latter is particularly sensitive to electron bombardment, beam-induced decomposition takes place more rapidly. The characteristic M-dot contrast is lost, leading to poor

contrast along the fault. This makes the direct observation of larger chain widths than those already characterized much more difficult. However, large decomposed lamellae are rarely observed: it seems that, in response to compositional fluctuation, large, multichain defects are less preferentially accommodated than single-, quadruple- and especially triple-chain faults.

(vii) *Regular triple-chain structure*

Occasionally, triple chains may order over sufficient distance to contribute sharp reflections to diffraction patterns. Recently, others (Veblen *et al.* 1977) have reported and characterized ordered triple-chain silicate minerals; in figure 12*a* (plate 11) we show an ordered triple-chain structure coherently intergrown with amphibole. The lattice image contains a sharp boundary (arrowed), to the left of which the (020) spacing, *ca.* 9 Å, corresponds to the double-chain amphibole structure and to the right of which the periodicity is $1\frac{1}{2}$ times this, i.e. 13.5 Å, with the contrast indicating regular triple chains. A double-chain 'fault' at A interrupts the otherwise perfect sequence. The simulated image contrast, figure 12*b* (plate 11), is as expected – two rows of bright fringes (coalesced M dots) running down the chain centres. The (0*kl*) selected area diffraction pattern from a larger part of the crystal (figure 12*c*, plate 12) contains mainly amphibole reflections, but the extra spots (arrowed) on rows parallel to b^* are those from the triple-chain structure; the periodicity in reciprocal space is $\frac{2}{3}$ that of the amphibole, and every second spot along b^* is a coincident reflection from both structures. Examination of the micrograph by selected area optical diffractometry (Millward & Thomas 1975) effectively separates this pattern into two discrete reciprocal lattice nets from each of the two phases (figure 12*d* and *e*, plate 12). This method was also used to determine whether there was any variation in lattice spacings adjacent to planar faults; no significant variation, however, was detected.

The triple-chain structure should possess the ideal composition, $Ca_2(Mg, Fe)_8Si_{12}O_{32}(OH)_4$, with expected unit cell parameters *a*, *c* and β very close to those of nephrite but with *b* being *ca.* 27.3 Å. A mineral that is broadly of this type has been named clinojimthompsonite by Veblen *et al.* (1977). The difference in composition between such a new phase and that of its nephrite host should be detectable by X-ray microanalysis of the specimen in the microscope. In practice, however, difficulties arise in that (*a*) regular triple chains occur only rarely and (*b*) when they are present, their extent is so small that the probe size (diameter between 1000 and 2000 Å) largely encompasses unfaulted nephrite, so that only small deviations away from the bulk composition can be detected. This latter effect is even more of a problem with irregularly faulted crystals.

Typical analyses from two of the nephrites, as determined by electron microprobe and X-ray emission microanalysis, are given below (figures quoted to within ± 5%).

Silesian nephrite

(*a*) electron microprobe: Si, 8.28; Al, 0.12; Fe, 0.49; Mn, 0.05; Ca, 2.03; Mg, 4.69;
(*b*) X-ray emission based on Si ≡ 8.0: Al, 0.07; Mg, 4.88; Ti, 0.05; Cr, 0.05; Fe, 0.47; Ca, 2.00.

Rhodesian nephrite

(*a*) electron microprobe: Si, 8.31; Al, 0.05; Cr, 0.02; Fe, 0.45; Mn, 0.03; Mg, 4.82; Ca, 1.99;

(*b*) X-ray emission based on Si ≡ 8.0: Mg, 4.64; Ca, 1.98; Ti, 0.05; Cr, 0.02; Mn, 0.02; Fe, 0.65.

(Idealized formula $Ca_2(Mg, Fe)_5Si_8O_{22}(OH)_2$.)

(viii) *Terraced defects*

Just as surfaces are terraced, so also can planar faults exhibit similar irregularities: figure 13 (plate 13) shows such an occurrence in nephrite. The triple-chain defect A–B, instead of continuing throughout the crystal, as is usually the case, steps sideways and down through the crystal (BC) by some six (020) spacings and returns again parallel to AB at CD. The angle of progression sideways is at *ca.* 120° to [001] and the sudden termination of the fault line AB causes an antiphase of the (020) fringes across the region BC. Figure 14 (plate 14) represents a possible structural scheme to explain this phenomenon in terms of an idealized chain structure in which the double chains form hexagonal rings.

The triple-chain AB can, because of its hexagonal structure, progress sideways through the crystal at an angle of 120°, thereby generating a multi-linked chain structure, in effect a strip of talc, BC. The triple chain is regained in a similar fashion (CD). It is clear that the generation of such a strip implies that only alternate double chains abutting on the region can match in orientation the tetrahedra in the strip (see figure 1*b*). Where double chains E, F, G and H (which have their tetrahedra pointing into the paper, as opposed to those of the 'talc' strip, which are pointing outwards) join the strip, inversion of tetrahedra through the edge-sharing of the two linking tetrahedra is postulated. Undoubtedly, the layers of cations separating the chains will be disrupted: the arrangement drawn involves minimal disruption.

(ix) *Defect terminations and dislocations*

Occasionally, complex, but local, structural changes involving planar faults are seen. Often these involve fault terminations, together with anomalous contrast effects. Good quality images are essential for the elucidation of complicated structures.

Figure 15 (plate 15) shows two adjacent triple-chain defects (A and B) and a single chain (C) at the lower part of the micrograph. The upper part of the micrograph, however, shows only defect A, both B and C having 'merged' into the normal amphibole structure, a fact confirmed by the phase relations of the (001) fringes: across A and B together they are in phase and are antiphase across C. Very gradually, as C is eliminated, its antiphase relation disappears, while simultaneously, as B expands to form two double chains, its own antiphase relation likewise vanishes. The portion of the crystal surrounding all these extraordinary changes evidently experiences no strain: it remains, in the sense previously used, 'antiphase' overall at the top and at the bottom, and the total number of chains remains the same. Note also how, as B and C vanish simultaneously, there is a subtle bending of only those M-dots in between the fault lines of B and C.

A model devised to account for these structural changes is shown schematically in figure 16. Here the chains of linked tetrahedra are represented by solid strips, trapezoidal in cross section, indicating whether the tetrahedra are pointing up or down. The inter-layer cations have been omitted for clarity. At the left, triple chain B at the front splits into two adjacent double chains towards the rear, requiring the insertion of an extra chain. In order to preserve the required up-down-up-down sequence of tetrahedra in adjacent chains (see figure 1*b*), it is necessary for the two newly-created double chains, which must of necessity have their tetrahedra pointing

in the same sense, to separate and occupy different positions along the [100] axis. In reality, this 'dislocation' must possess a screw character with Burgers vector $\frac{1}{2}[100]$. In a similar fashion, defect C terminates within the crystal – in its wake it cannot leave two adjacent double chains with tetrahedra pointing in the same sense – this situation being relieved with a further screw dislocation possessing an identical Burgers vector, but of opposite sense.

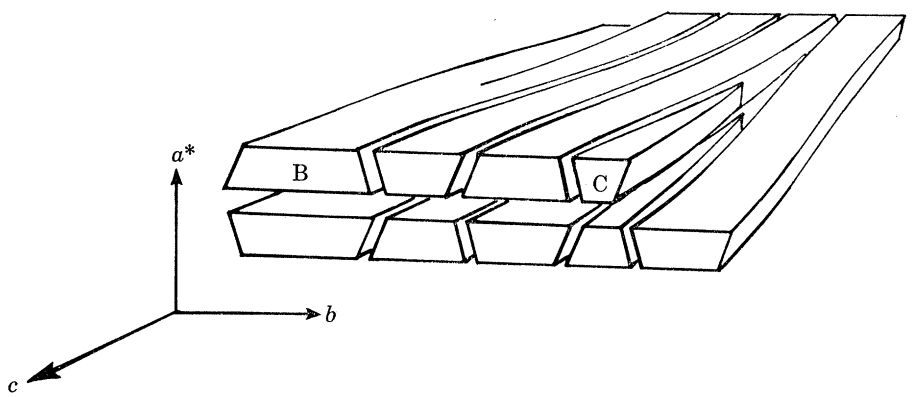

FIGURE 16. Schematic structural interpretation of the fault terminations shown in figure 15. The silicate chains are represented by strips, trapezoidal in cross section.

It can be seen from figure 15 that the M-dot contrast between faults B and C is enhanced with respect to the surrounding image, the shape of the dots indicating a slight orientational difference. The canting of the central slab of structure produced by the two boundary screw displacements could indeed have this effect, fortuitously bringing the lattice into better alignment.

In this model we have assumed that the dislocations are parallel to [100]. This, of course, need not be so, although the remarkable clarity of the lattice images suggests that any deviation from this direction would be small. The dislocations are similar to features occasionally observed in complex oxide block structures, for which a detailed analysis has been published (Anderson *et al.* 1976). Such partial screw dislocations are here postulated to be a feature of chain silicates. It was not possible to attempt a systematic analysis of the dislocations by using either diffraction contrast techniques (Hirsch *et al.* 1965) or titled images (Iijima & Buseck 1975) since beam damage precluded such an extended examination. Moreover, the small size of the unit cell in reciprocal space would demand an excessively small objective aperture for good diffraction contrast.

The edge components of the fault complex are, it seems, complementary, producing no distortion in the overall surrounding crystal. Notwithstanding the dangers of too literal an interpretation of lattice image fringe bending (Cockayne *et al.* 1971), we nevertheless attach significance to this feature, and a detailed model depicting the termination of defect C is proposed in figure 17.

A further, analogous example of fault termination is shown in figure 18 (plate 16). At the lower part of the micrograph A and B are two adjacent quadruple-chain defects, while C is a single chain. Proceeding upwards along the [001] direction B 'splits' to form a double chain and a triple chain, while defect C is simultaneously eliminated. Again, the overall odd (001) fringe phase relation is maintained, and as many chains are created as are lost, with no resulting

distortion of the surrounding structure. That an exactly analogous situation prevails to that previously described is shown by the similar degree of fringe bending and contrast enhancement – a similar model to that of figure 16 would be appropriate for this fault complex.

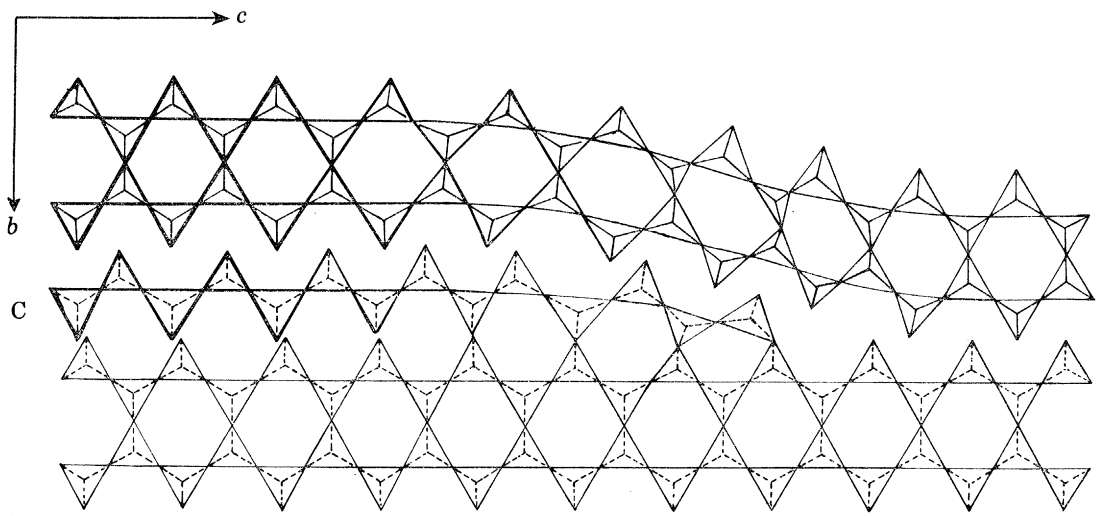

FIGURE 17. A proposed structure for the termination of single chain C in figures 15 and 16, involving a five-membered silicate ring.

5. SUMMARY AND CONCLUSIONS

The fact that a variety of amphiboles contain structural irregularities in the form of (010) planar defects has been well established; usually such faults occur as the insertion of triple-chain lamellae within the double-chain host. The Chisholm (1975) interpretation of the amphibole structure as a crystallographic shear structure derived from pyroxene means that such lamellae can be regarded as Wadsley defects; this description then readily encompasses the occurrence of other multi-chain faults, and such faults with chain widths varying from one to six tetrahedra have been shown to exist in nephrite. Computational procedures for the calculation of lattice images have proved invaluable in the characterization of those faults for which other possibilities exist: six single chains could, for example, have been present rather than a sextuple chain. Image simulations have shown that, with care, intuitive interpretation of a faulted amphibole lattice image is indeed possible, since, under certain conditions, observed image contrast is a faithful representation of the crystal structure.

This confirmation implies that more complex features of the microstructure may also be simply interpreted. Into this category fall those defects which, unlike the majority, do not progress linearly throughout the crystal. Our analysis of chain termination within the amphibole matrix indicates that defect termination can be accommodated with little strain to the surrounding structure if it is closely linked to a similar termination in such a way that the total number of chains is conserved. In addition, it seems necessary under certain circumstances for the crystal to possess a rather special kind of screw dislocation, with a Burgers vector perpendicular to the chain axis and with its core at the termination. The presence of such a dislocation preserves the structural interrelation of the silicate chains. These relations do not appear inviolable, however, and the linkage of chains with opposing orientations through the edge-sharing of tetrahedra, thereby also disturbing the interlayering cations, remains a possibility.

More work, involving imaging under even higher resolution, is required before the nature of the linear defects that may be accommodated in these defects is further clarified.

The incorporation of multiple-chain defects within the amphibole matrix is necessarily accompanied by a local change in composition. No evidence exists for the incorporation of more than one single chain at a time (i.e. a strip of n single chains). Overall chemical trends seem to favour the incorporation of multiple-chain defects, implying lowered calcium and raised magnesium and iron concentrations. But while triple chains are frequent, quadruple and higher order chains become progressively rarer, and no septuple or wider chains have been found. On average, the deviation of whole nephrite crystals from actinolite stoichiometry is found to be small.

The recognition of ordered triple-chain regions within nephrite crystals implies a significant departure in composition from that of the amphibole. There are indications, however, that the transition between the double- and triple-chain structures may not always be abrupt. We have observed microregions containing two adjacent triple chains; we have also seen highly disordered regions containing many triple chains. Unfortunately, our microanalysis techniques are not yet sufficiently refined spatially to sample solely those regions of greatest structural interest. Small strips consisting of ordered triple chains are, at present, inaccessible. Likewise, it has not proved possible to detect any variation in crystal composition within the perfect amphibole adjacent to defects, although optical diffraction studies have indicated that there is no perceptible change in lattice spacings.

The structural problems posed in the interpretation of lattice fringe images of defects within amphiboles appear to have been largely solved. However, solutions to other problems, such as small scale variation in chemical composition, await the refinement of experimental techniques.

We acknowledge with gratitude the advice and guidance of Dr A. C. Bishop and Dr J. E. Chisholm (British Museum), and the cooperation of Dr G. R. Millward, Mr J. L. L. Jenkins and Mr E. L. Smith. This work, which was carried out at the Edward Davies Chemical Laboratories, University College of Wales, Aberystwyth, was supported by the Science Research Council, who awarded one of us (L.G.M.) a CASE studentship in association with the British Museum (Natural History).

References

Anderson, J. S. 1973 *J. chem. Soc. Dalton Trans.* p. 1107.
Anderson, J. S. & Tilley, R. J. D. 1974 *Surface and defect properties of solids* (ed. M. W. Roberts & J. M. Thomas), vol. 3, p. 1. London: The Chemical Society.
Anderson, J. S., Hutchison, J. L. & Lincoln, F. J. 1977 *Proc. R. Soc. Lond.* A **350**, 303.
Bursill, L. A. & Hyde, B. G. 1972 *Prog. Solid St. chem.* **7**, 178.
Buseck, P. R. & Iijima, S. 1974 *Am. Miner.* **59**, 1.
Chisholm, J. E. 1973 *J. Mater. Sci.* **8**, 475.
Chisholm, J. E. 1975 *Surface and defect properties of solids* (ed. M. W. Roberts & J. M. Thomas), vol. 4, p. 126. London: The Chemical Society.
Cockayne, D. J. H., Parsons, J. R. & Hoelke, C. W. 1971 *Phil. Mag.* **24**, 139.
Cowley, J. M .& Moodie, A. F. 1957*a* *Acta crystallogr.* **10**, 609.
Cowley, J. M. & Moodie, A. F. 1957*b* *Proc. Phys. Soc.* B **70**, 505.
Cowley, J. M. 1975 *Diffraction Physics.* Amsterdam: North Holland.
Erickson, H. P. & Klug, A. 1971 *Phil. Trans. R. Soc. Lond.* B **261**, 105.
Evans, E. L. & Thomas, J. M. 1975 *J. Solid St. Chem.* **14**, 99.
Evans, E. L., Jenkins, J. L. & Thomas, J. M. 1972 *Carbon* **10**, 637.
Goodman, P. & Moodie, A. F. 1974 *Acta crystallogr.* A **30**, 280.

Grinton, G. R. & Cowley, J. M. 1971 *Optik* **34**, 221.
Heide, H. G. 1963 *Z. angew. Phys.* **15**, 117.
Hirsch, P. B., Howie, A., Nicholson, R. B., Pashley, D. W. & Whelan, M. J. 1965 *Electron microscopy of thin crystals*. London: Butterworths.
Hutchison, J. L., Irusteta, M. C. & Whittaker, E. J. W. 1975 *Acta crystallogr.* A **31**, 794.
Hutchison, J. L., Jefferson, D. A., Mallinson, L. G. & Thomas, J. M. 1976 *Mater. Res. Bull.* **11**, 1557.
Hutchison, J. L., Jefferson, D. A. & Thomas, J. M. 1977 *Surface and defect properties of solids* (ed. M. W. Roberts & J. M. Thomas), vol. 6, p. 320. London: The Chemical Society.
Iijima, S. & Buseck, P. R. 1975 *Am. Miner.* **60**, 771.
Jefferson, D. A. & Thomas, J. M. 1974 *J. chem. Soc. Faraday Trans.* II **70**, 1691.
Jefferson, D. A. & Thomas, J. M. 1975 *Mater. Res. Bull.* **10**, 761.
Jefferson, D. A., Millward, G. R. & Thomas, J. M. 1976 *Acta crystallogr.* A **52**, 823.
Jefferson, D. A. & Thomas, J. M. 1977 *Abstracts of Fourth European Crystallographic Meeting* (Oxford), B 626.
Jefferson, D. A. & Thomas, J. M. 1978 *Proc. R. Soc. Lond.* A **361**, 399.
Jefferson, D. A. & Thomas, J. M. 1979 *Acta crystallogr.* A **35** (in the Press).
Jefferson, D. A., Mallinson, L. G., Hutchison, J. L. & Thomas, J. M. 1978 *Contrib. Miner. Petrol.* **66**, 1.
Kittel, C. 1978 *Solid St. Commun.* **25**, 519.
Lynch, D. F. & O'Keeffe, M. A. 1972 *Acta crystallogr.* A **28**, 506.
Lynch, D. F., Moodie, A. F. & O'Keeffe, M. A. 1975 *Acta crystallogr.* A **31**, 300.
Mallinson, L. G. 1976 M.Sc. thesis, University College of Wales, Aberystwyth.
Mallinson, L. G., Hutchison, J. L., Jefferson, D. A. & Thomas, J. M. 1977 *J. chem. Soc. Chem. Commun.*, 910.
Millward, G. R. & Thomas, J. M. 1975 *Proceedings of the Fourth London International Carbon and Graphite Conference*, p. 492. (Society of Chemical Industry, London).
Mitchell, J. T., Bloss, F. D. & Gibbs, G. V. 1971 *Z. Kristallogr. Kristallgeom.* **133**, 273.
Papike, J. J., Ross, M. & Clark, J. R. 1969 *Miner. Soc. Am. Spec. Pap.* **2**, 117.
Rodgers, G. L. 1969 *J. Microsc.* **89**, 121.
Spence, J. C. H. 1976 *Developments in Electron Microscopy and Analysis* (ed. J. A. Venables), p. 257. New York: Academic Press.
Thomas, J. M. & Jefferson, D. A. 1978 *Endeavour* (New Series) **2**, 127.
Thomas, J. M. 1974 *Phil. Trans. R. Soc. Lond.* A **277**, 251.
Thomas, J. M., Millward, G. R., Davies, N. C. & Evans, E. L. 1976 *J. chem. Soc. Dalton Trans.* p. 2443.
Thomas, J. M. 1977 *Chem. Br.* **13**, 175.
Thompson, J. B. Jr 1970 *Am. Miner.* **55**, 292.
Thompson, J. B. Jr 1978 *Am. Miner.* **63**, 239.
Veblen, D. R., Buseck, P. R. & Burnham, C. W. 1977 *Science, N.Y.* **198**, 359.
Wadsley, A. D. 1964 In *Non-stoichiometric Compounds* (ed. L. Mandelcorn). New York: Academic Press.
Wadsley, A. D. & Andersson, S. 1970 *Perspectives in Structural Chemistry* (ed. J. D. Dunitz & J. A. Ibers), vol. 3. New York: Wiley.

b

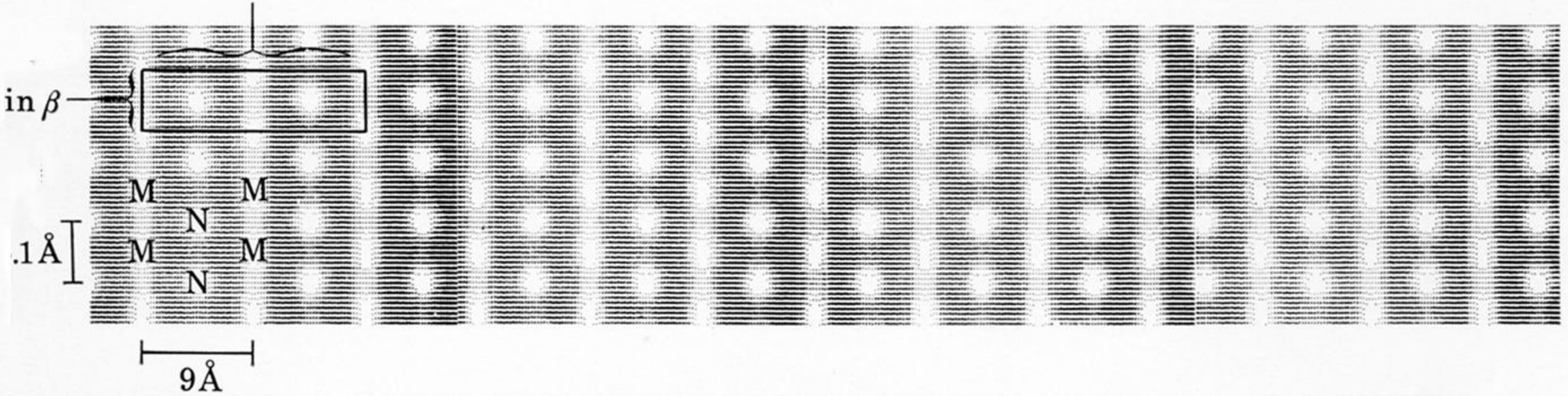

FIGURE 2. Computed, (0*kl*) elcctron microscope images of actinolite (*a*) and tremolite (*b*), for a crystal 100 Å thick and a defocus of 1000 Å. The notation used to describe image features in the text is indicated. (Non-uniformity of intensity in some areas is entirely due to line-printer faults and does not represent real variation.)

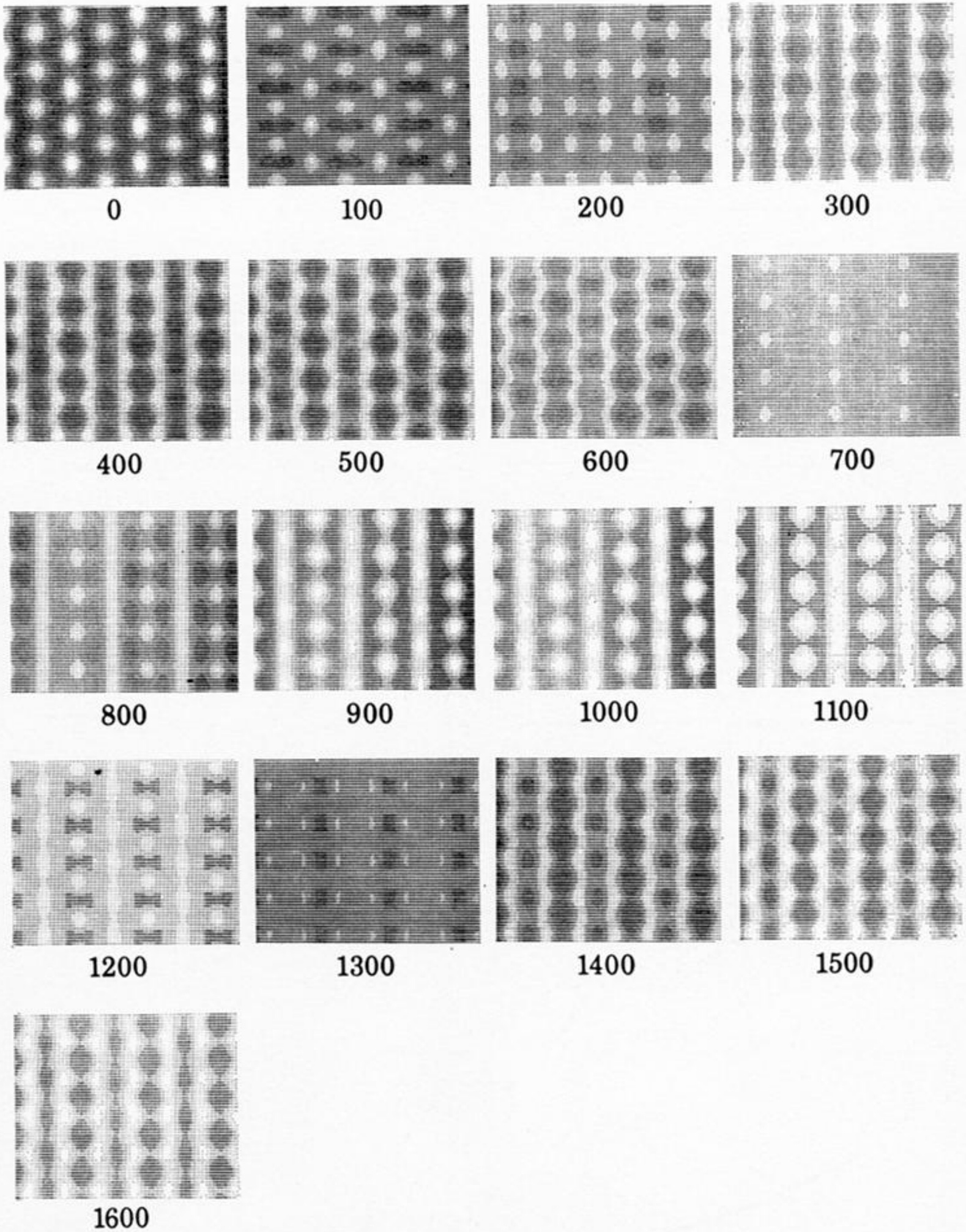

FIGURE 4. Computed images of tremolite, projected down [100], with defocus values from 0 to 1600 Å, for a crystal 100 Å thick. The image can be interpreted directly in terms of the crystal structure at defocus values around 1000 Å.

FIGURE 3. Computed images of tremolite projected down [100] at thicknesses H from 2.5 to 1000 Å and at defocus values DF from 900 to 1200 Å. Note how the region of interpretable image contrasts shifts from a defocus around 900 Å at a crystal thickness of 2.5 Å to around 1200 Å at a thickness of 400 Å.

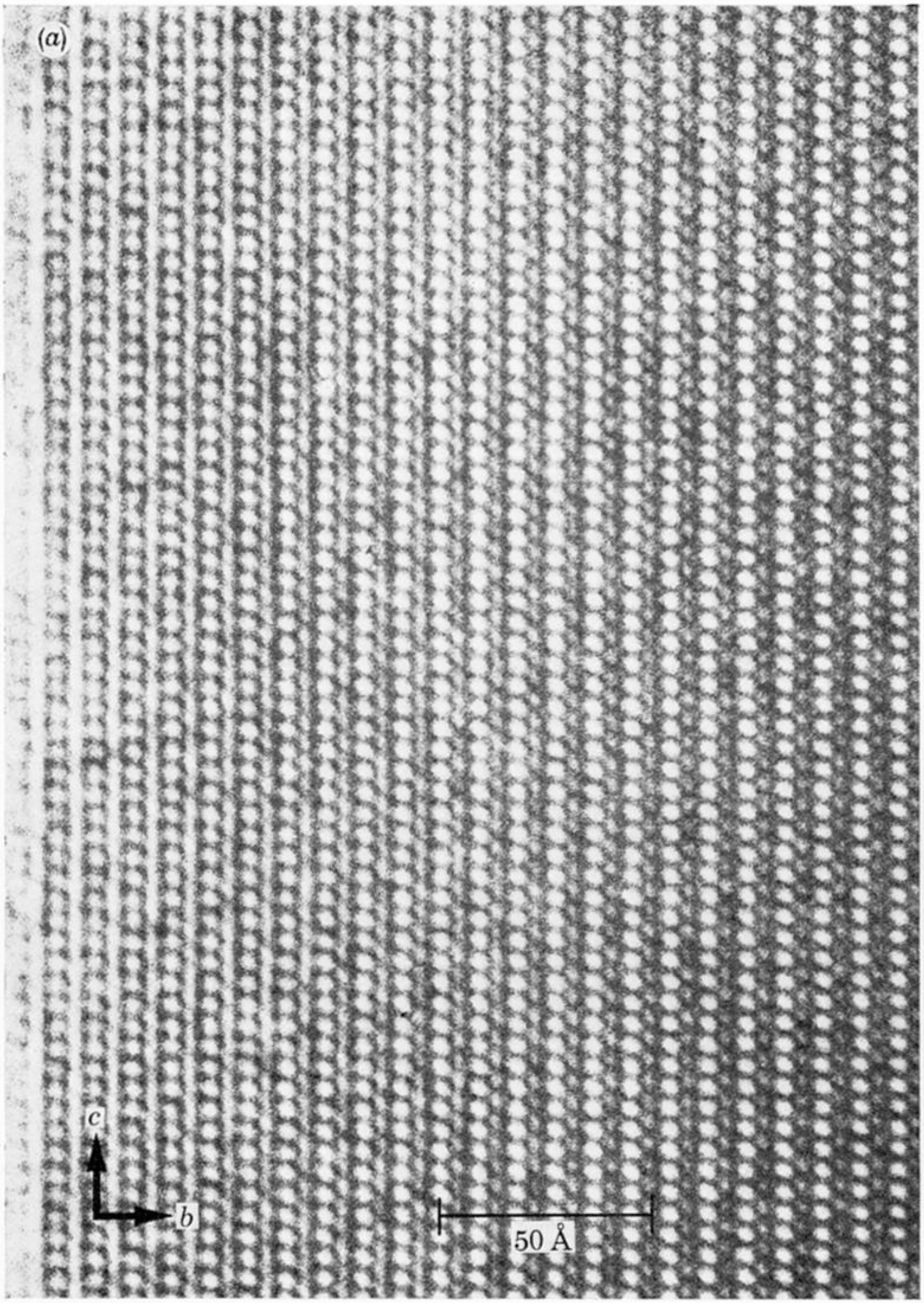

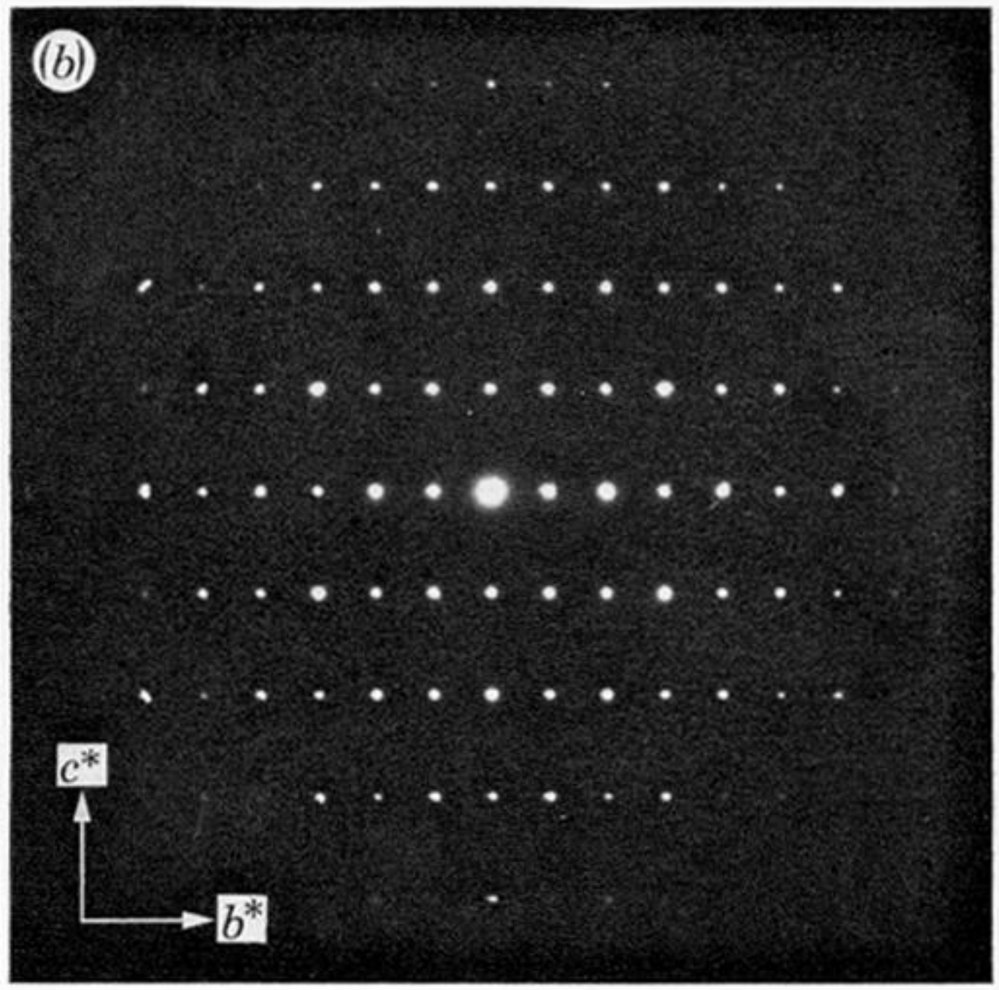

FIGURE 5. (*a*) Structural image from a portion of a crystal of Silesian nephrite, with the electron beam parallel to [100]. The crystal increases sharply in thickness from the edge, at the left, where the image matches those computed at thicknesses up to 500 Å, while towards the right-hand side the contrast closely resembles that computed for 750 Å thick crystals (see figure 3). (*b*) A (0*kl*) electron diffraction pattern from a nephrite crystal orientated precisely so that the beam is parallel to the [100] axis of the crystal.

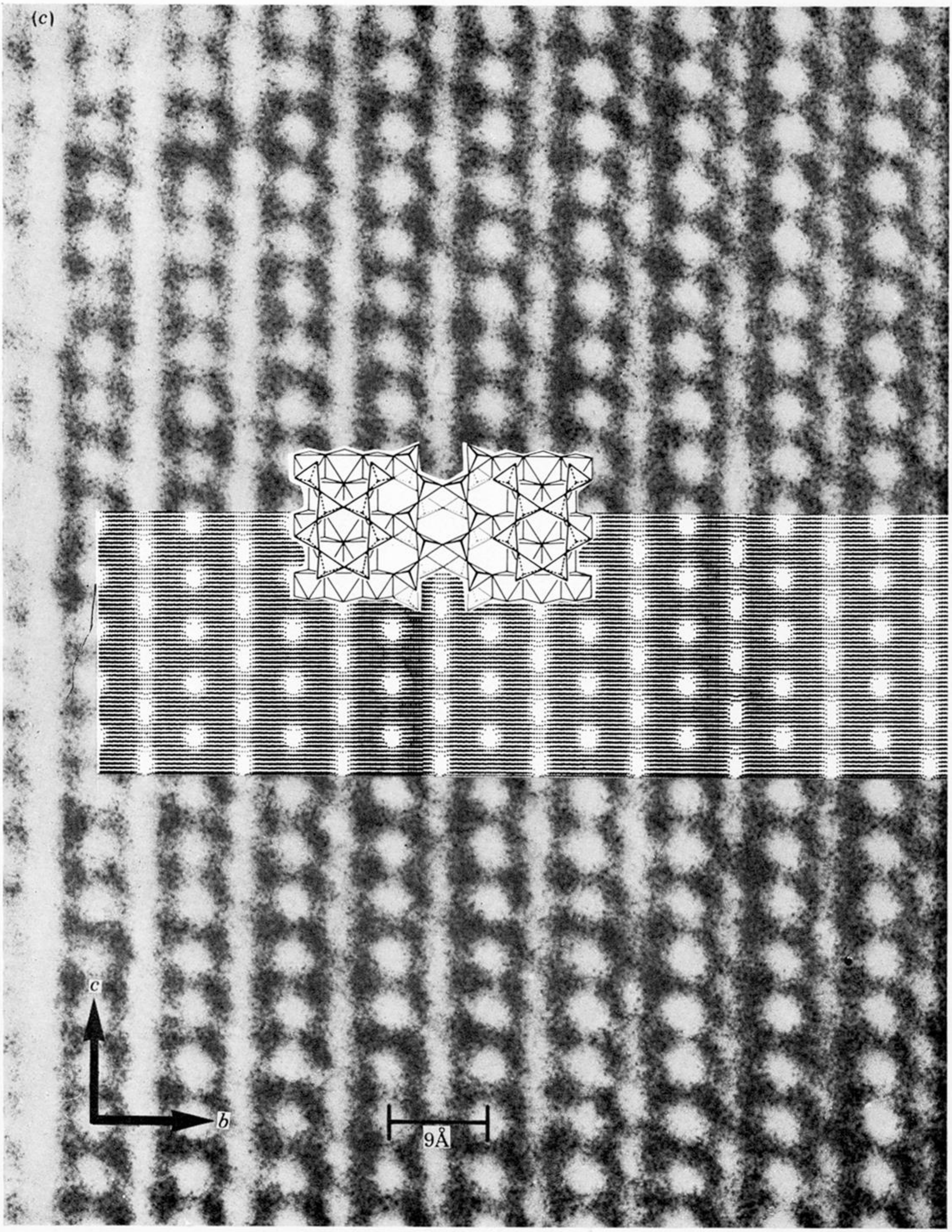

FIGURE 5. (*c*) A section of the image in (*a*) enlarged to show the match with a calculated image (for a crystal 100 Å thick and at a defocus of 1000 Å) and the amphibole structure.

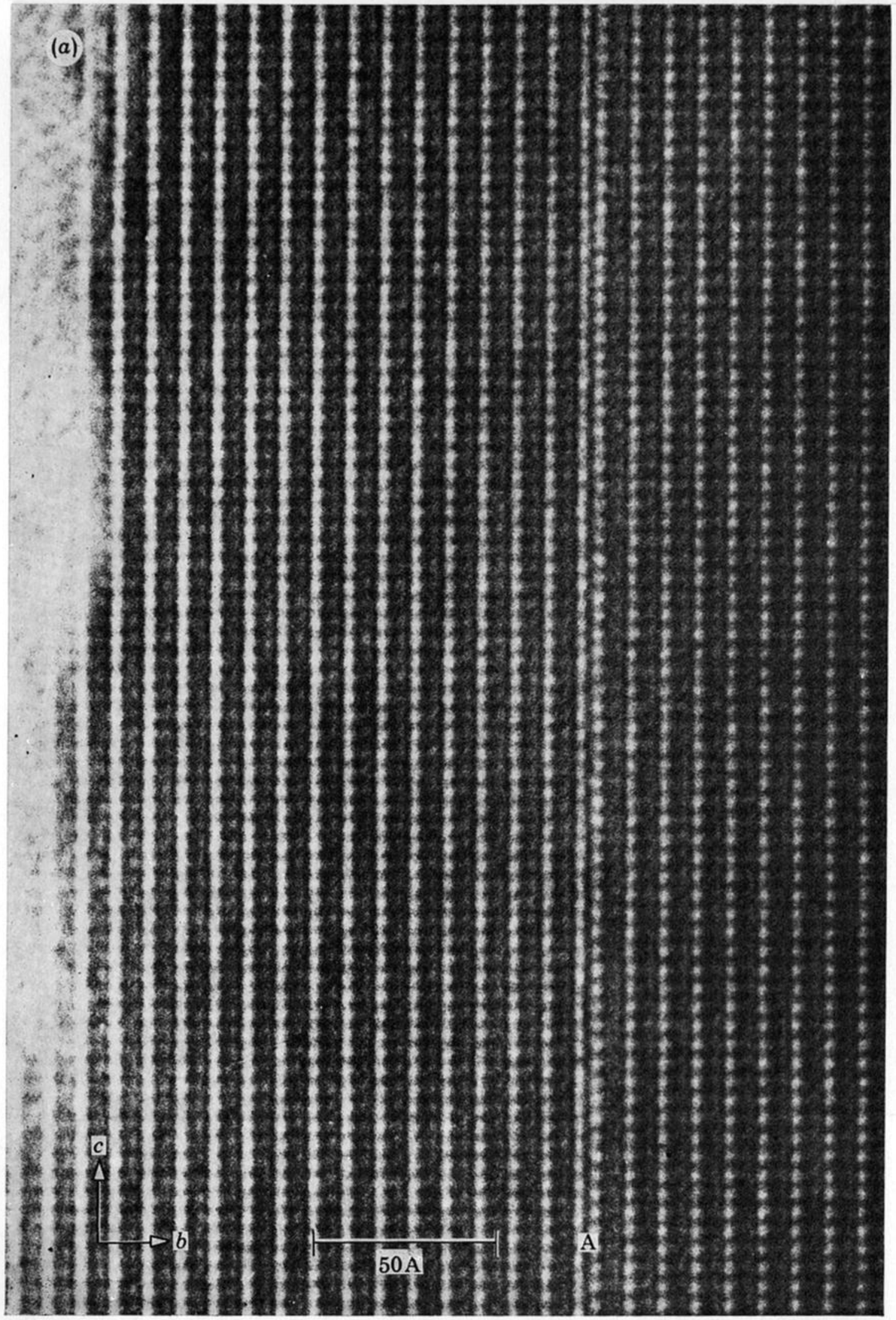

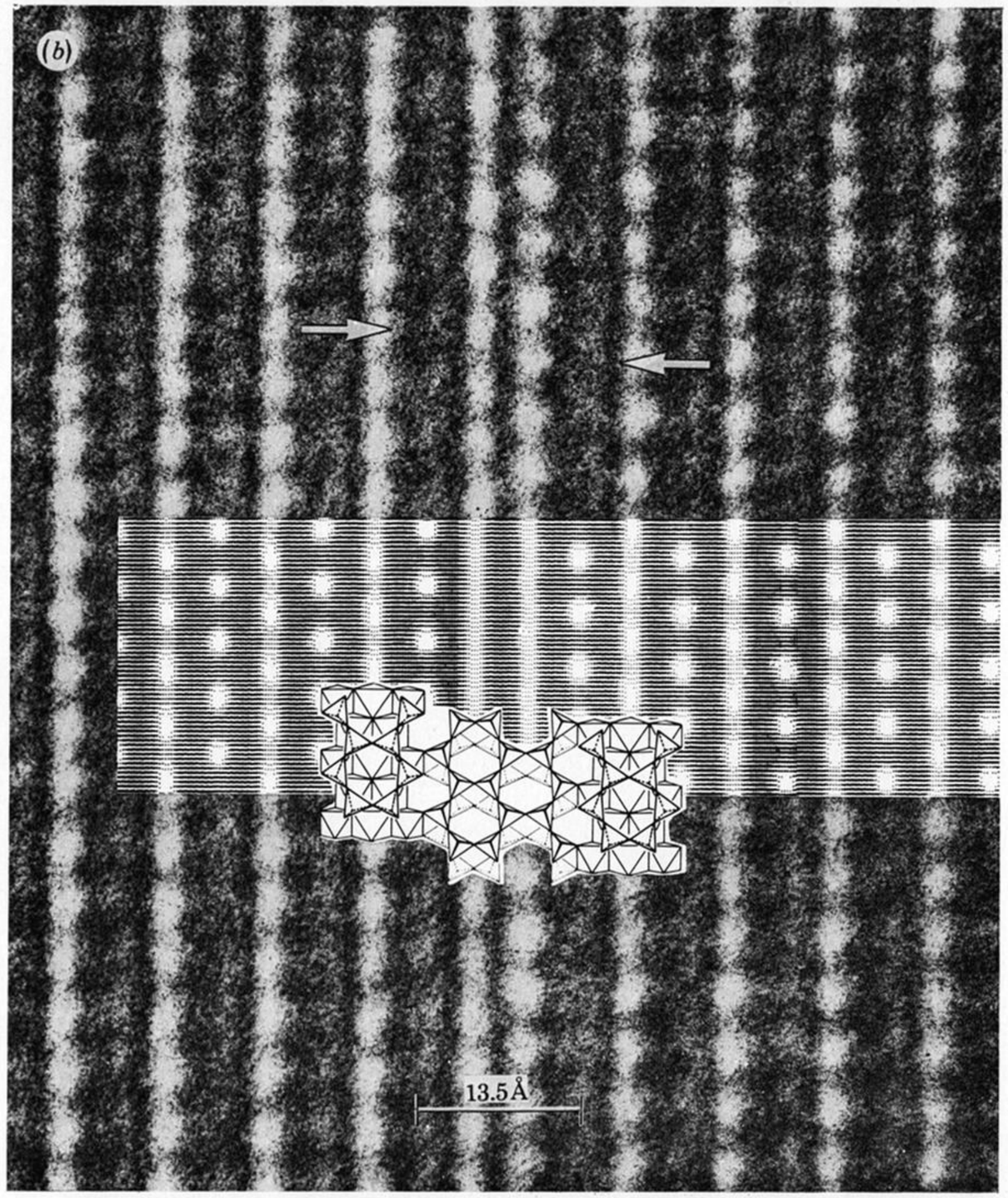

FIGURE 6. (*a*) A triple-chain defect at A near the edge of a crystal of nephrite from Rhodesia. (*b*) A portion of (*a*) matched with a computed image (thickness 100 Å, defocus 1000 Å) and the proposed defect structure. The antiphase of the (001) fringes across the fault is indicated by the arrows.

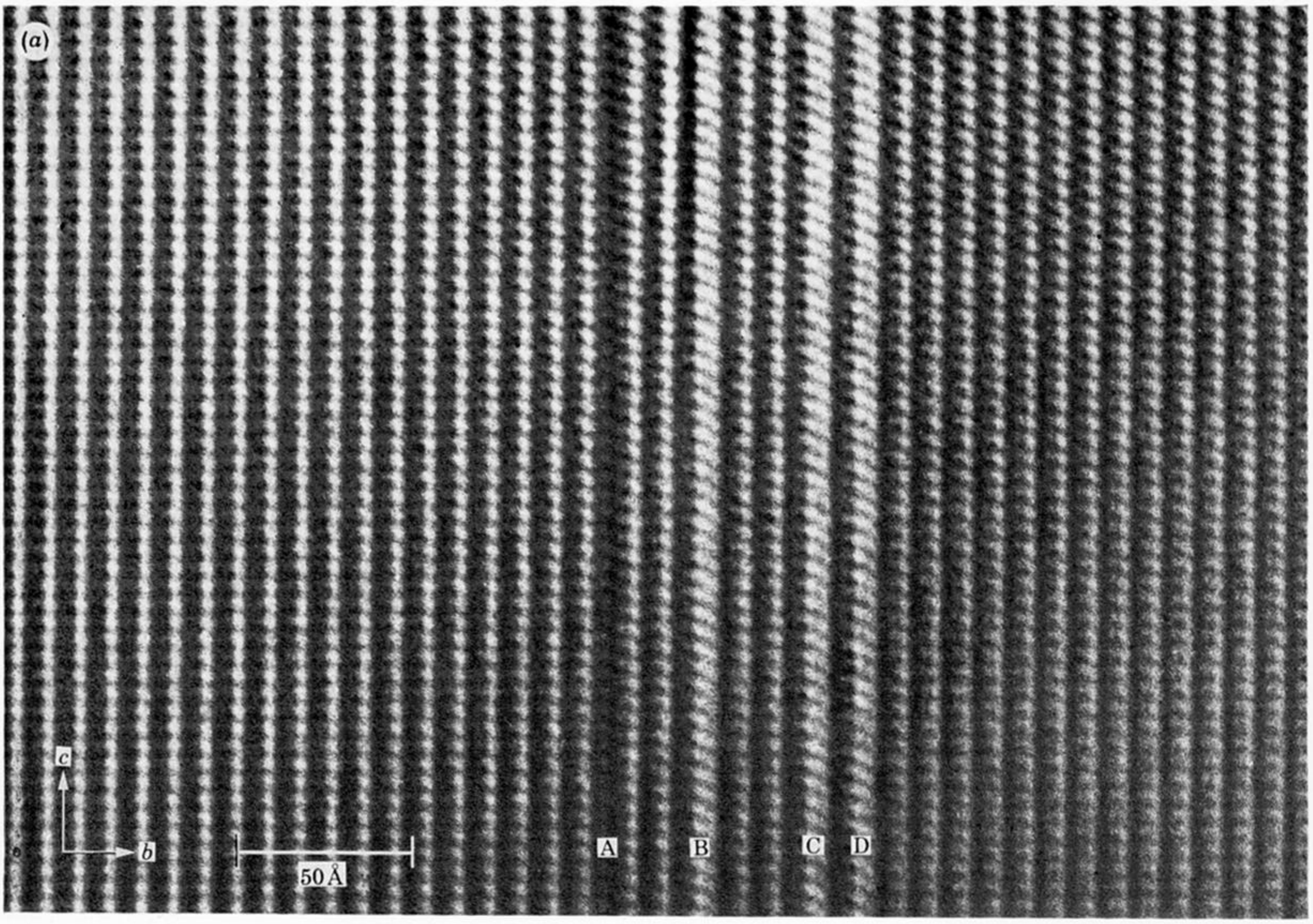

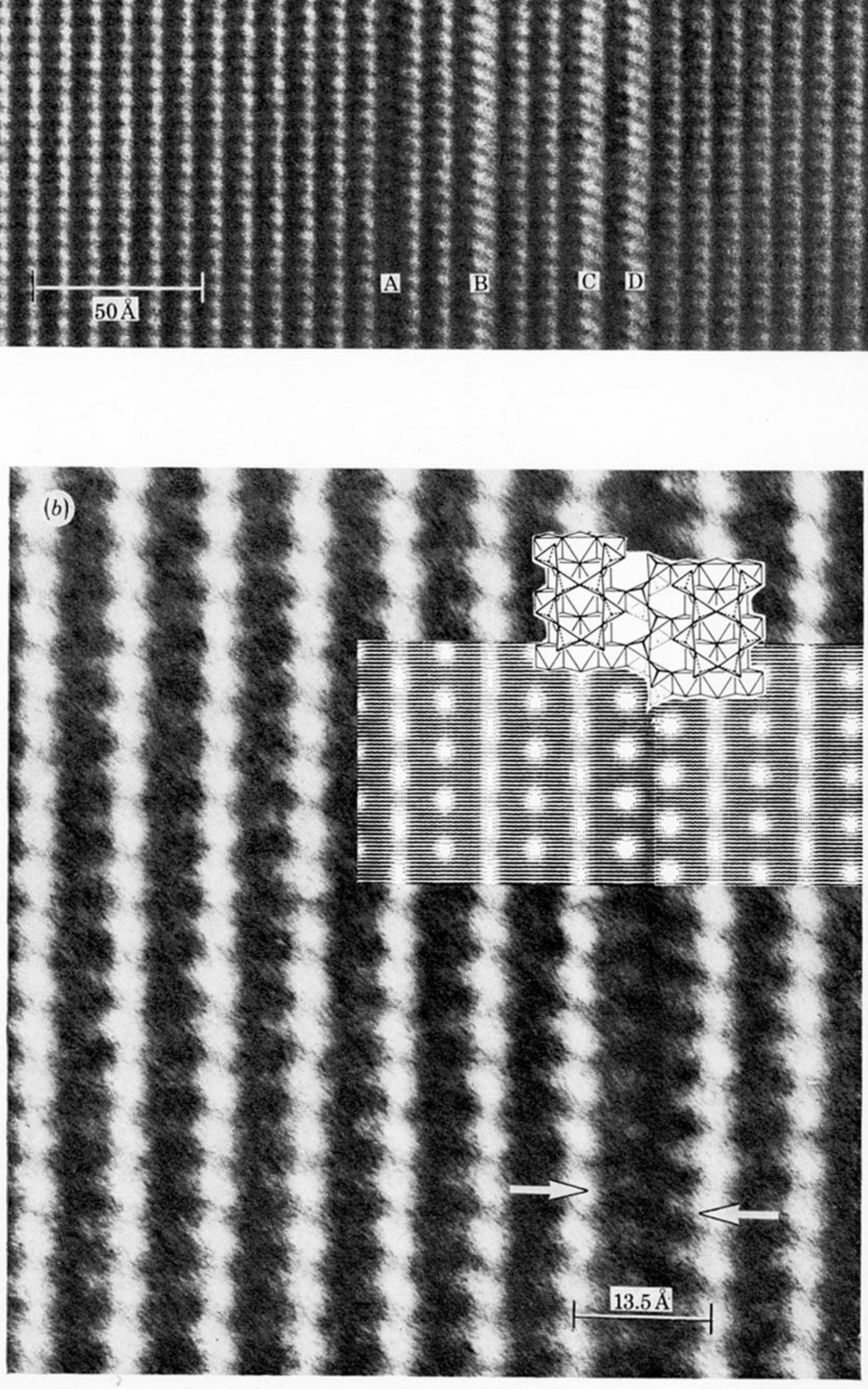

FIGURE 7. (*a*) A single chain present (in Rhodesian nephrite) in the double-chain matrix at A can be compared with three triple chains at B, C and D. (*b*) An enlargement of (*a*) shows the matching with an image computed for a single chain defect (100 Å thick, defocus 1000 Å), together with the structural interpretation on the same scale.

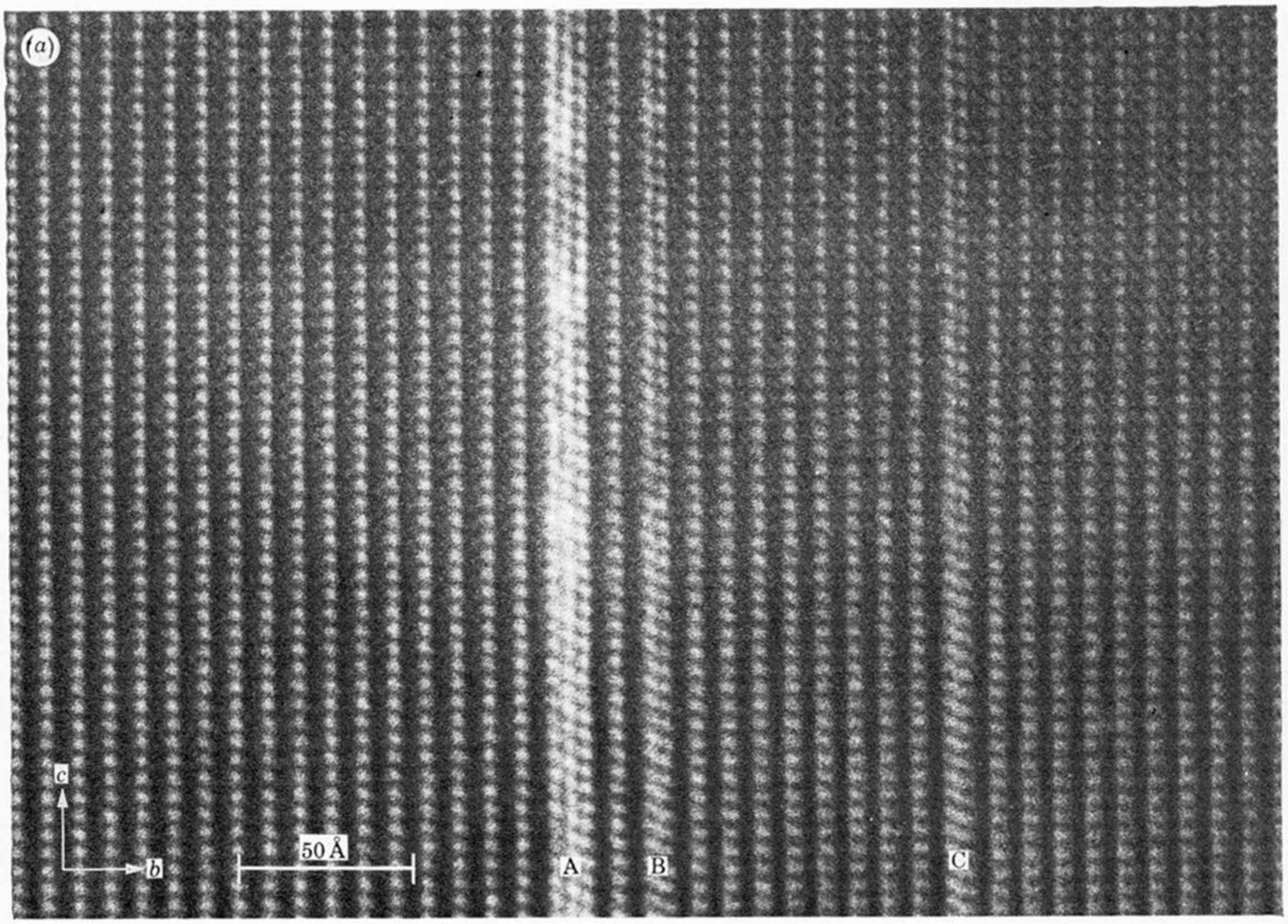

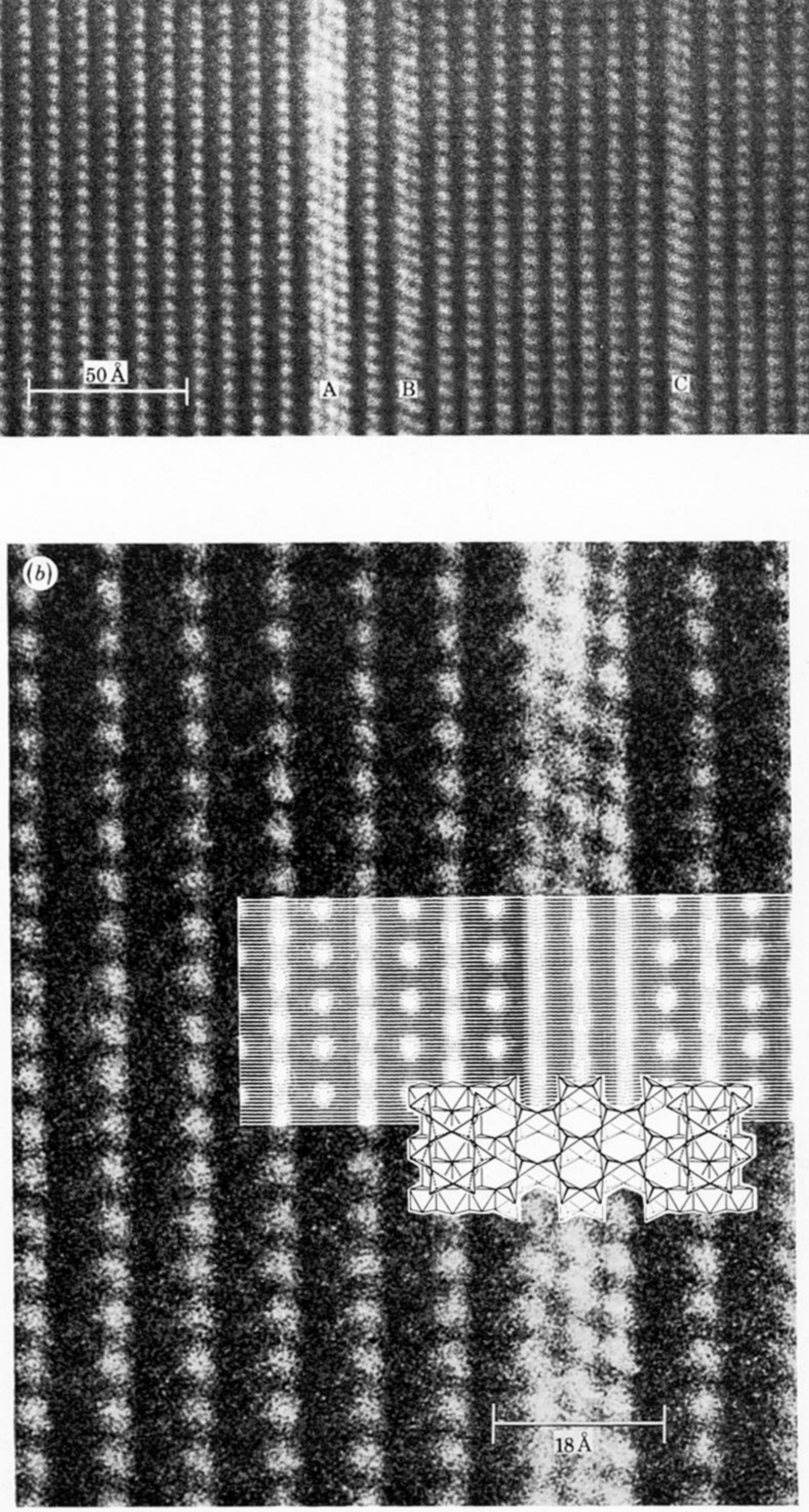

FIGURE 9. (*a*) Rhodesian nephrite with a quadruple chain defect at A, together with two triple chains, B and C, intergrown with amphibole. (*b*) An enlargement of A is compared with an image computed for a quadruple chain fault (thickness 100 Å, defocus 1000 Å), together with the proposed structure on the same scale.

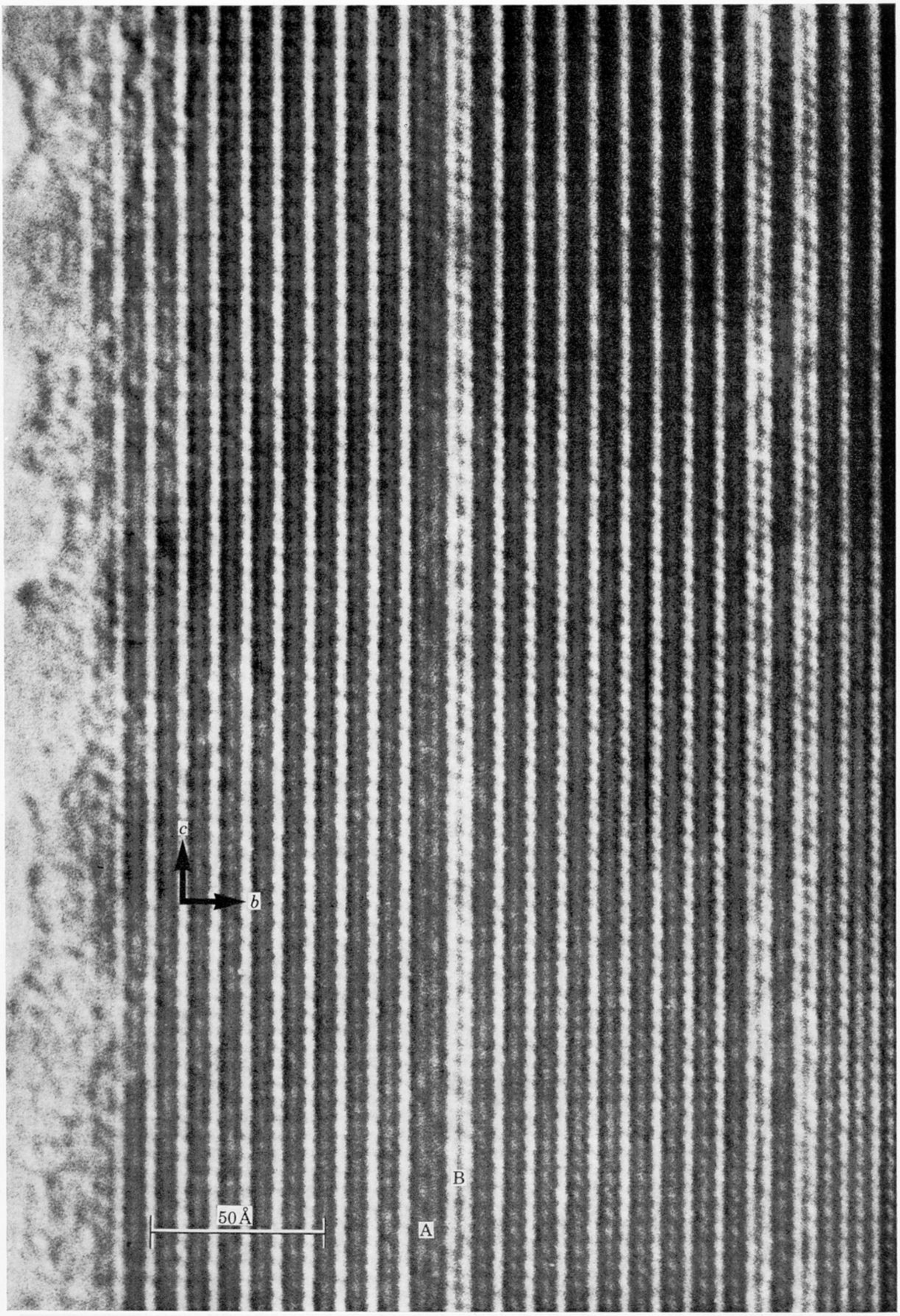

FIGURE 8. Rhodesian nephrite with a single chain (A) and a triple chain (B) occurring side by side in the amphibole matrix. Two adjacent triple chains can also be seen on the right.

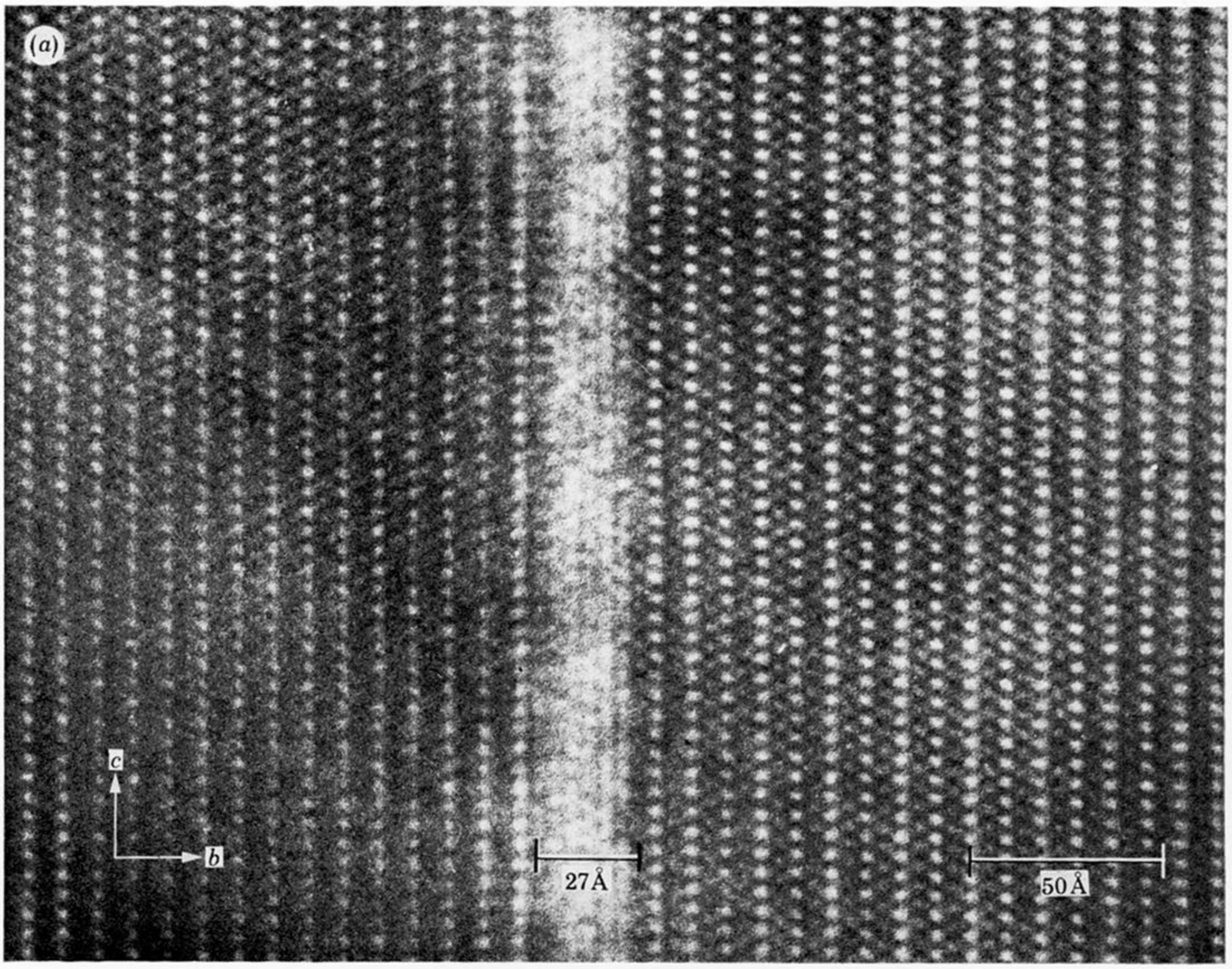

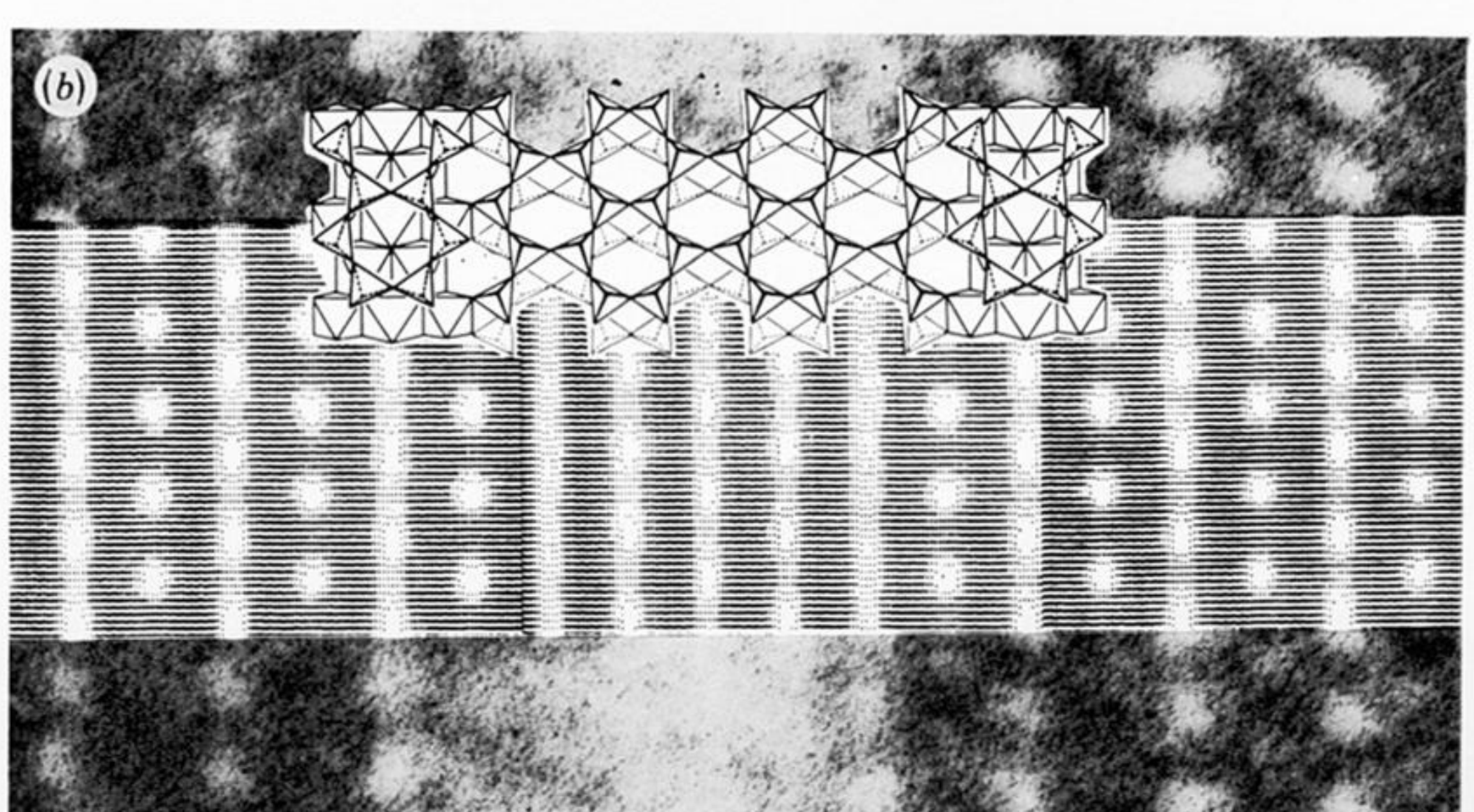

FIGURE 10. (*a*) A sextuple chain defect in New Zealand nephrite. (*b*) An enlargement of (*a*) showing matching with a computed image (thickness 100 Å, defocus 1000 Å) and the proposed structure. Note the tendency of the fault to suffer greater beam damage than the surrounding matrix.

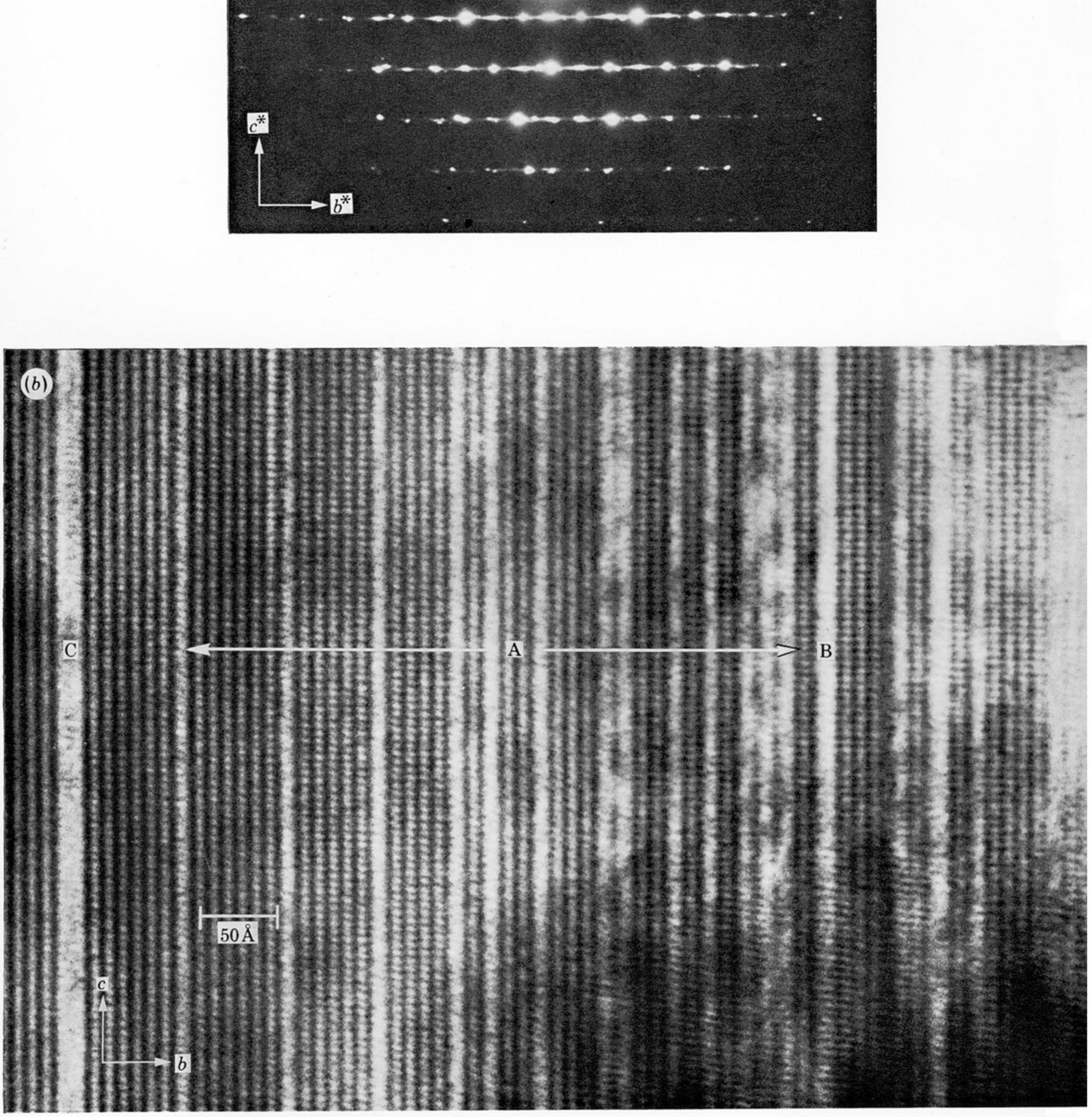

FIGURE 11. (*a*) A (0*kl*) electron diffraction pattern from a crystal of Rhodesian nephrite, showing extensive streaking along lines parallel to *b**. (*b*) The high degree of disorder indicated in (*a*) is manifest in the lattice image which shows an array of triple chains (A), a quadruple chain (B), and a possible quintuple chain (C).

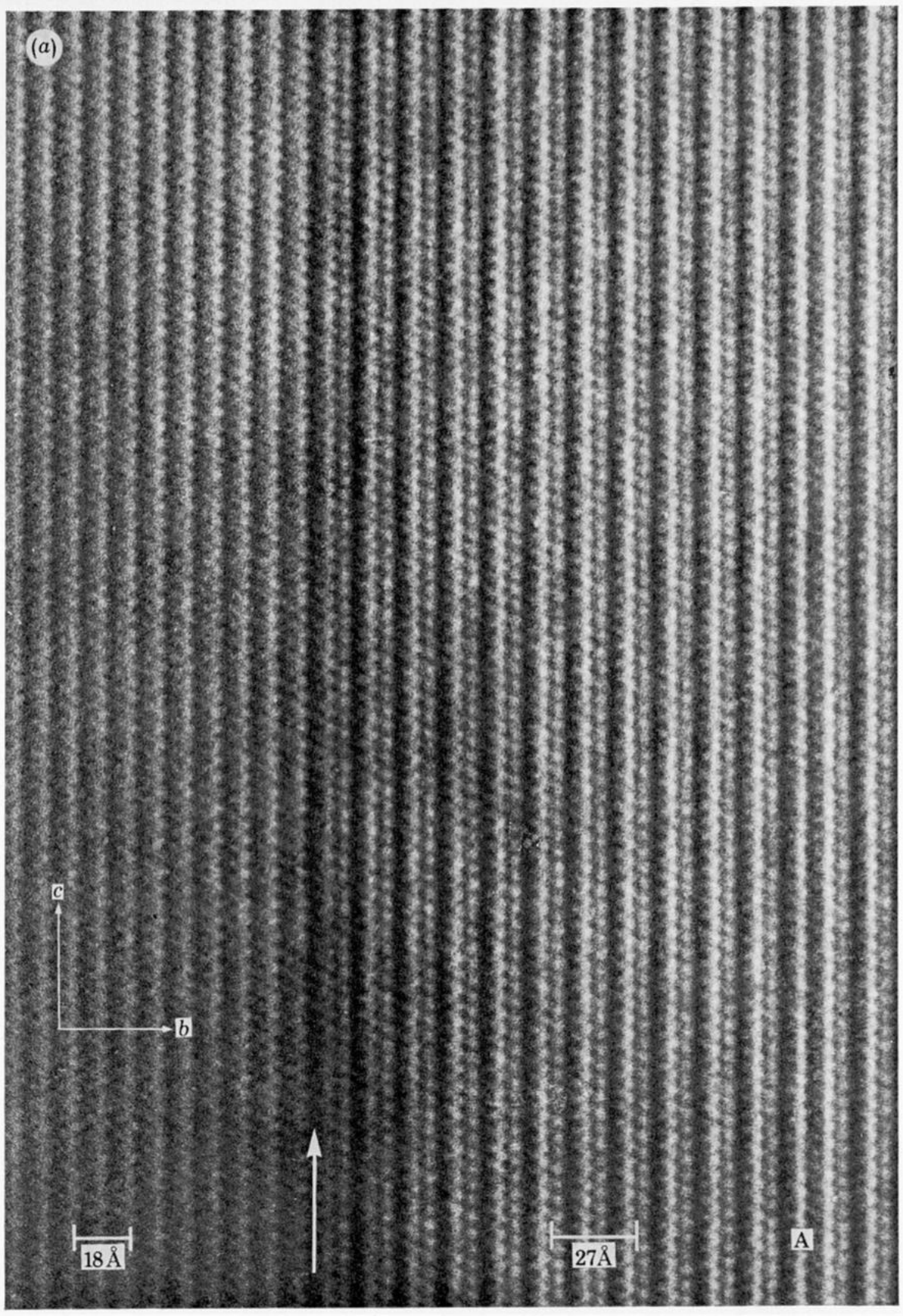

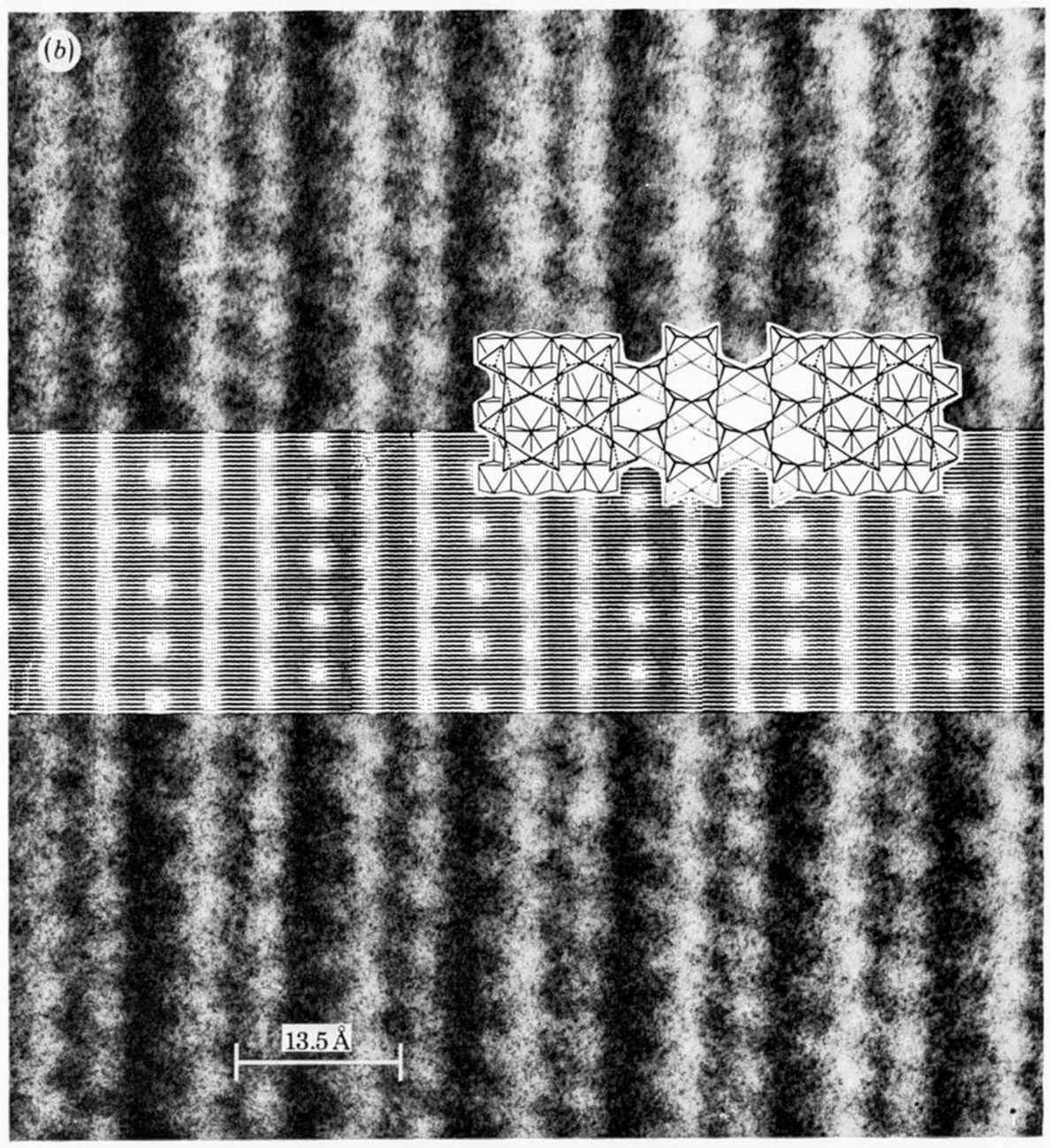

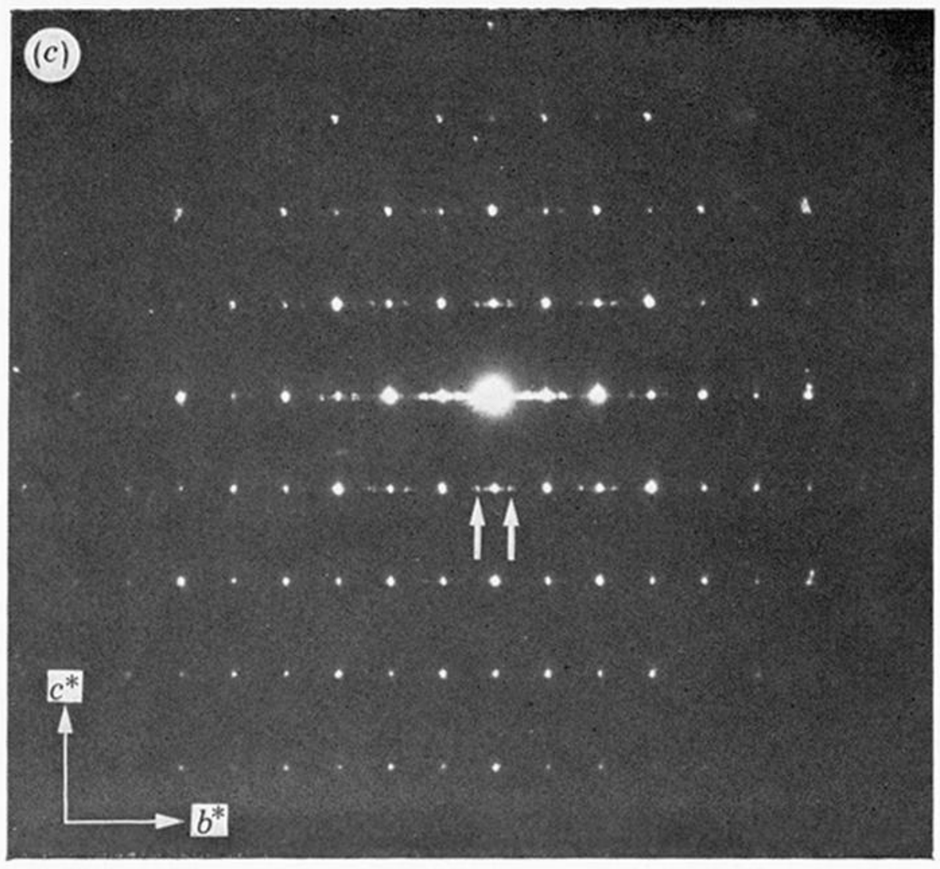

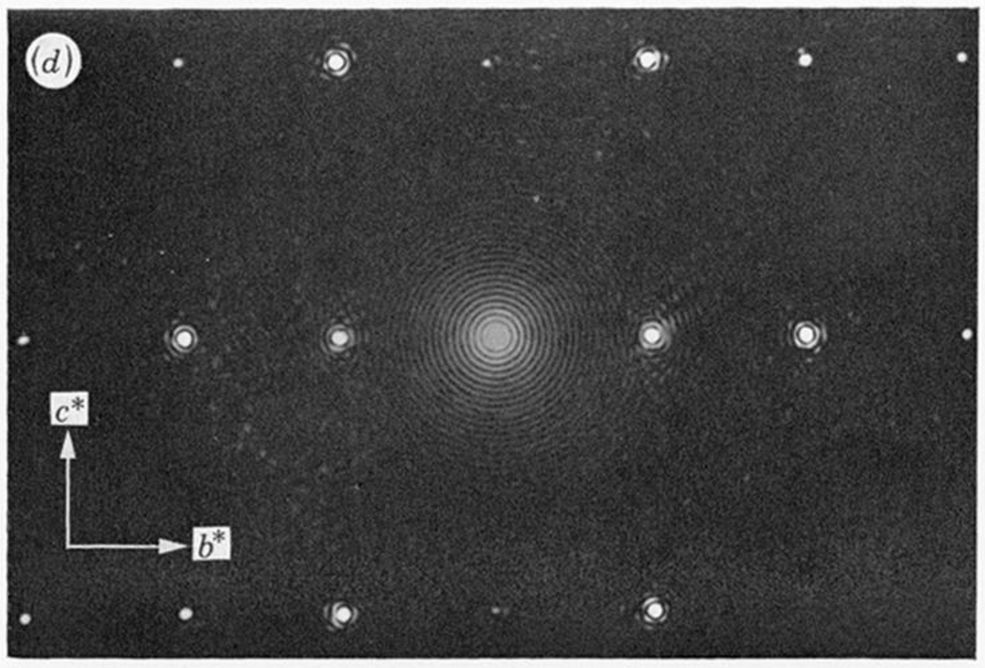

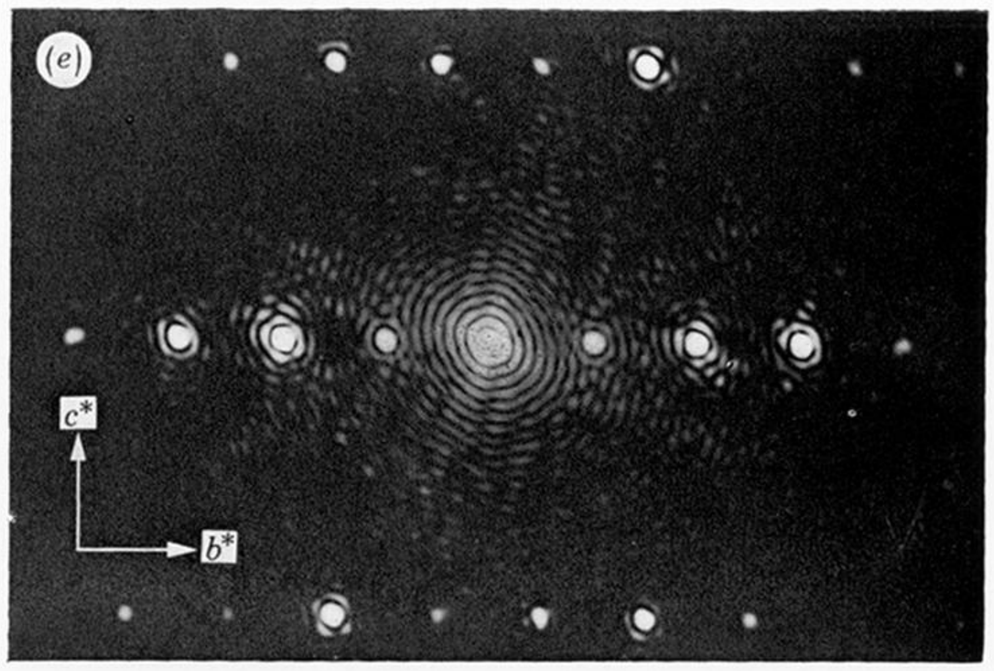

FIGURE 12. (*a*) Image from a crystal of Rhodesian nephrite showing an intergrowth of amphibole (on the left) with a structure comprising regular triple chains (on the right). A is a double-chain 'fault'. (*b*) An enlargement of (*a*) showing the match with a computed image (thickness 100 Å, defocus 1000 Å) and the proposed triple-chain structure. (*c*) A (0*kl*) electron diffraction pattern from the nephrite crystal incorporating the regular triple chains, containing extra reflections (arrowed) from the new structure. (*d*) An optical diffraction pattern from the left-hand side of (*a*) shows the

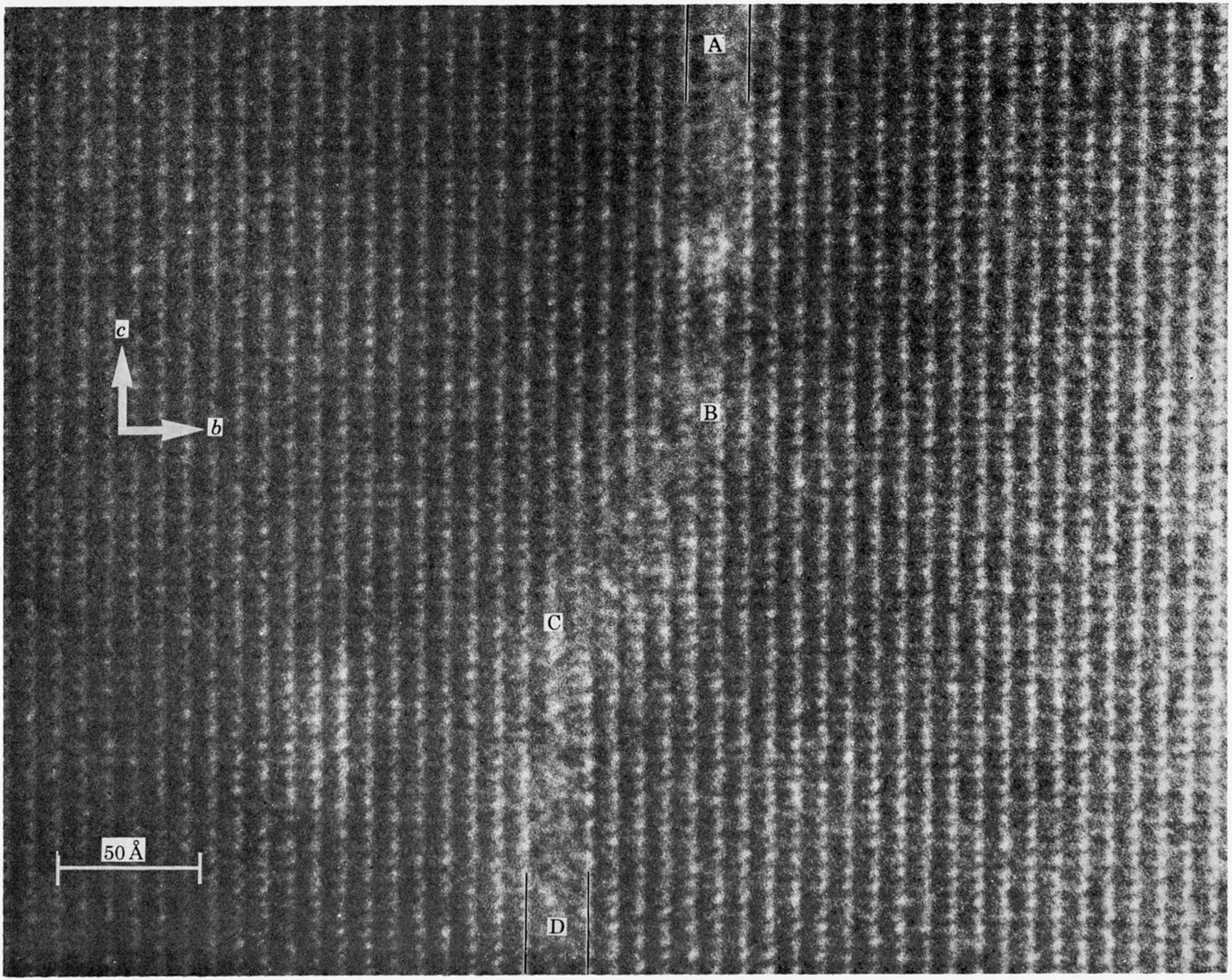

FIGURE 13. A triple-chain defect A–B, in a crystal of Californian nephrite, alters position in the crystal to C–D. The (020) fringes across the region B–C are in antiphase, best seen by viewing along DA.

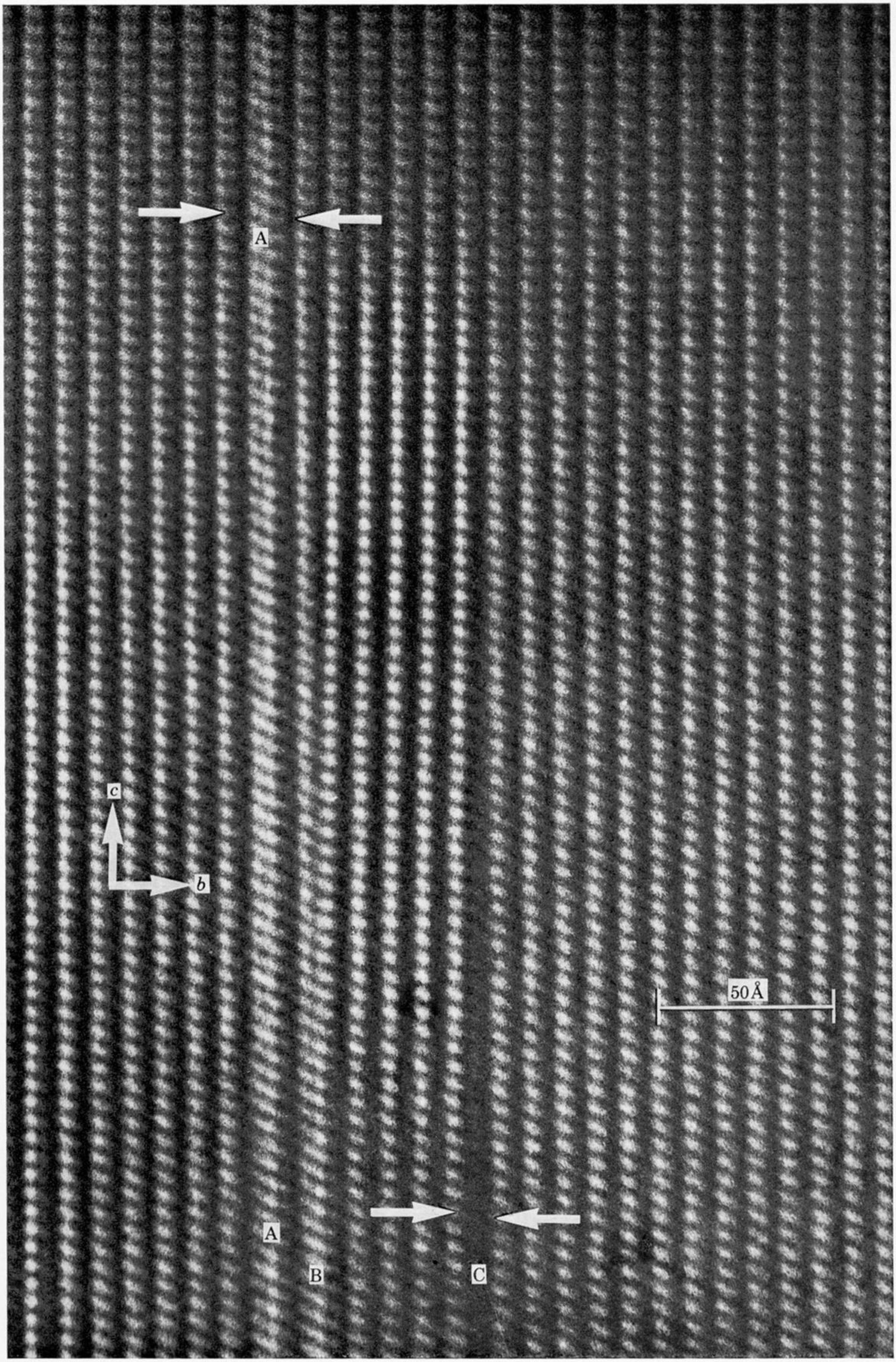

FIGURE 15. Two associated defect terminations in a nephrite crystal from the Rhodesian sample. Triple chain B and single chain C in the lower half are eliminated in the middle region and are not present in the upper half. The (020) fringes in the region between the two gradual terminations are bent and the contrast enhanced.

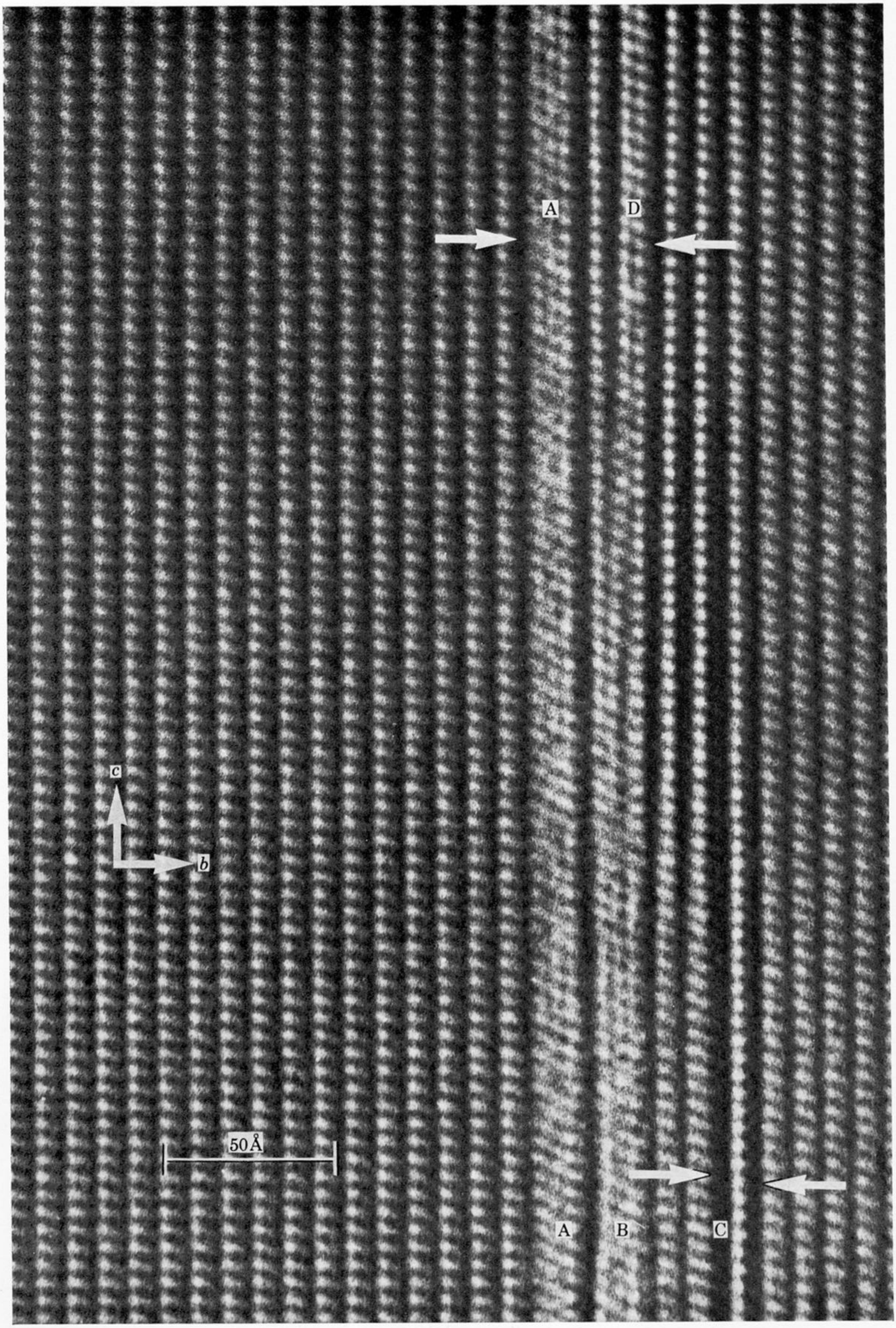

FIGURE 18. Another type of fault termination in Rhodesian nephrite. Two quadruple chains A and B and a single chain C are present in the lower half of the micrograph. Towards the upper half B is transformed into a triple chain D and C is eliminated. The region between the terminations shows fringe bending and anomalous contrast.